Schweizerische Eidgenossenschaft
Confédération suisse
Confederazione Svizzera
Confederaziun svizra

Department of the Environment, Transport,
Energy and Communication DETEC

Swiss Federal Office of Energy SFOE
Energy Research and Cleantech Section

Final report dated 28.01.2022

Grid-forming control of renewable generation and power electronics

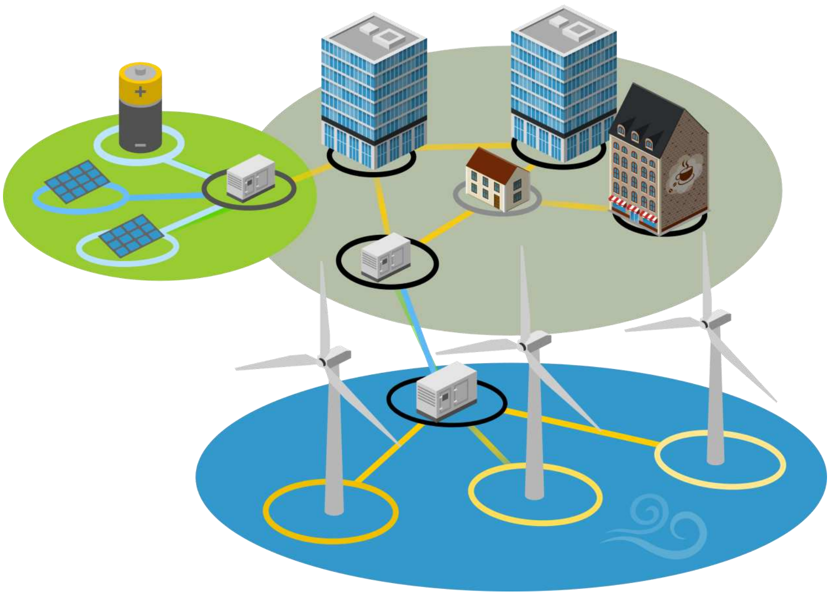

GREAT

Date: 28.01.2022

Location: Bern

Publisher:
Swiss Federal Office of Energy SFOE
Energy Research and Cleantech Section
CH-3003 Bern
www.bfe.admin.ch

Subsidy recipients:
ETH Zürich, Automatic Control Laboratory
Physikstrasse 3, 8092 Zürich
control.ee.ethz.ch

Author:
Dominic Groß, University of Wisconsin-Madison (formerly ETH Zürich), dominic.gross@wisc.edu
Irina Subotić, Automatic Control Laboratory, ETH Zürich subotici@control.ee.ethz.ch

SFOE project coordinators:
Dr. Michael Moser, michael.moser@bfe.admin.ch

SFOE contract number: SI/501707

Summary

The electric power system is undergoing an unprecedented transformation towards massive integration of renewable generation interfaced by power electronics. A key challenge of this transition is the replacement of conventional thermal power plants and their synchronous generators by distributed renewable generation connected to the grid through power electronic converters. Ever decreasing costs of photovoltaics and wind turbines make large-scale deployments of renewable generation very appealing. However, using standard grid-following (GFM) control with maximum power point tracking, the impact of renewable integration on frequency stability of electric power systems is highly problematic. Today's grid operation heavily relies on bulk generation and synchronous machines that provide significant amounts of rotational inertia, maintain self-synchronization through the power network, and ensure stable and reliable operation of the power system through their frequency and voltage control. While various power electronic devices can be used to emulate machine inertia, this class of heuristic control algorithms does not leverage the fast actuation capabilities of power converters and, as documented by recent studies may be inefficient or even fail to stabilize a grid dominated by power electronics. A key technology to overcome this challenge are grid-forming (GFM) power converters that control the voltage magnitude and frequency at their converter terminal to ensure self-synchronization and grid stability. While the significant advances have been made towards replacing synchronous machines with grid-forming power converters current works focus on studying networks of power converters but typically neglect the power source feeding the converter. The main objective of this project is to develop novel unified control framework that fully leverage the capabilities of power converters, renewable generation (e.g., wind turbines and photovoltaics), energy storage systems, and other common actuators (e.g., high-voltage DC transmission) for autonomous primary control and integrates with prevailing secondary control architectures. Because future power systems are envisioned to contain millions of distributed devices centralized coordination on the time scales of primary control is neither desirable nor viable. Therefore, this project aims to develop control algorithms that ensure a high level of self-organization of the system.

Main findings

- The key dynamics of emerging technologies (e.g., photovoltaics, wind power, high-voltage DC) and existing technologies (e.g., synchronous machines and synchronous condensers) at the system level can captured in a unified reduced order modeling framework.
- A universal control paradigm has been developed that unifies standard functions of grid-following (GFL) and GFM (e.g., primary frequency control, maximum power point tracking) in a single universal controller and is backwards compatible with conventional machine-based generation and prevailing secondary control architectures.
- The fast primary frequency control response of curtailed renewable generation technologies and power electronics can be used to replace the fast inertia response and slow primary control response of conventional synchronous machine-interfaced generation.

Contents

1 Introduction **5**

1.1 Background information and current situation 5

1.2 Purpose of the project 6

1.3 Objectives 6

2 Procedures and methodology **7**

3 Results and discussion **8**

3.1 Modeling of power generation, power conversion, and power transmission 8

3.2 Control and small-signal stability analysis framework 19

3.3 Secondary control 32

3.4 Flexibility and short-term energy storage of converter-interfaced renewable generation 34

4 Conclusions **37**

5 Outlook and next steps **38**

6 Publications and Dissemination **38**

References **39**

1 Introduction

1.1 Background information and current situation

A major transition in the operation of electric power grids is the replacement of conventional power generation using synchronous machines by distributed generation based on renewable sources interfaced by power electronics. In contrast to synchronous machines, which stabilize the power system through a combination of their inherent physical properties, e.g., rotational inertia, and their controls, power converters do not inherently stabilize the power system. While the loss of rotational machine inertia has received significant attention in the literature [1, 2], it is just one of a multitude of stability challenges that arise [3].

In particular, today renewable energy sources that are interfaced by power electronics are controlled to maximize their power generation (so called maximum power point tracking) under the assumption that the voltage of their point of connection has constant frequency and amplitude irrespective of their power injection. The challenges that need to be overcome to fully leverage the potential by renewable power sources and energy storage systems can be broadly categorized according to their time scales. On the scale of hours, days, and seasons energy storage is required to overcome the cyclic nature (i.e., day-night cycles) and fluctuations in renewable generation. In contrast, the focus of this project is power system frequency stability on the scale of milliseconds to seconds. On this time-scale both the controls of power converters and controls of renewable resources interfaced by power electronics (e.g., wind turbines and solar photovoltaics) need to contribute to stabilizing the overall power system instead of soley maximizing their power generation.

Moreover, the level of grid-support provided by distributed and renewable generation strongly depends on the dynamics, static limitations (e.g., maximum power generation), and inherent energy storage (i.e., inertia of a wind turbine) of renewable power sources interfaced by the converter. For example, a power converter interfacing photovoltaics cannot provide primary or secondary frequency control without sufficient solar irradiation, but it can still provide frequency oscillation damping similar to a power system stabilizer (PSS). In addition, with sufficient DC terminal energy storage the power converter can provide an inertia response, and with sufficient irradiation and curtailment it can provide primary and secondary frequency control.

Control strategies for grid-connected power converters can be broadly categorized [4] into grid-forming strategies that form a stable AC voltage (i.e., magnitude and frequency) at the converter terminal but assume that the DC voltage is stable, and (ii) grid-following controls that form a stable DC voltage but assume that the AC system is stable. The two approaches are complementary in the sense that grid-forming requires a stable DC voltage (i.e., significant energy storage) and stabilizes the AC system, while grid-following control requires a stable AC system and stabilizes the DC voltage (e.g., to implement maximum power point tracking). Specifically, grid-following control can only operate in a system with sufficient number of synchronous generators and grid-forming devices [5] and is vulnerable to grid disturbances [6, 7], while grid-forming control fails if the converter DC voltage is not tightly controlled by a power source [8]. Thus, at present, a mix of grid-forming and grid-following control is needed to operate power systems that contain renewable generation and high-voltage DC transmission (HVDC) [9]. The resulting complex heterogeneous system dynamics pose significant challenges for system operation and stability analysis [5].

Grid-following control crucially depends on the assumption that the grid-voltage waveform is sinusoidal and its magnitude and frequency change slowly. Under this assumption a so called phase-locked-loop (PLL) is used to estimate the voltage frequency and phase angle at the point of connection and the power converter is controlled as a power source [10, 11]. In practice, the power injected is controlled to stabilize the converter power source at its maximum power point. Given some power source flexibility, the power injection can also be controlled to provide a response that is proportional to the estimated frequency and rate of change of frequency [12]. However, the resulting control is fragile and frequently fails when the power system is under stress. To the best of the authors knowledge, all major contingencies related to power electronics and renewable generation reported to date (e.g., [6], [7]) can ultimately be traced back to grid-following converter control. In contrast to common believe, these contingencies are not related to a loss of rotational inertia but the design assumptions of grid-following control.

As a consequence, grid-forming power converters are envisioned to replace synchronous machines as the cornerstone of future power systems. The prevalent approach to grid-forming control is droop-control [13, 14, 15]. Other approaches include synchronous machine emulation [16, 17], and virtual oscillator control [18, 19, 20, 21]. These control strategies control the power converter as a voltage source that forms a stable AC voltage at the point of connection and measures the converter power injection to mimic the self-synchronizing behaviour and $P-f$ droop of synchronous machines. While power converters with these controls can black-start a grid, provide primary frequency control, and can be extended to emulate machine inertia [12] and secondary control, they require that the power source on the DC terminal of the power converter can provide a stable DC voltage. Based on this assumption, all of the aforementioned studies investigate networks of the AC terminal of DC/AC power converters without modeling power generation explicitly. If controllability of the power source is lost (i.e., a renewable energy system reaches its maximum power point, or an energy storage system is depleted) or the power source cannot respond fast enough to stabilize the DC voltage, the converter will not fall back to providing the functionality that can be provided without power source (e.g., reactive power support and oscillation damping) but instead will destabilize the system [8]. While the requirement of sufficient control reserves is arguably less problematic than the drawbacks of grid-following control, it nonetheless poses a huge obstacle for participation of a wide range of devices in operating future power systems from renewable generation, energy storage, and high-voltage DC (HVDC) systems.

Finally, to the best of our knowledge, no scalable analytical stability analysis methods are available in the literature that cover conventional technologies (i.e., synchronous machines and synchronous condensers), the dynamics and limited controllability of renewables, and both power converters providing common grid-forming (e.g., primary frequency control) and grid-following functions (e.g., maximum power point tracking). Considering that numerical approaches (e.g., [5]) do not scale beyond a few hundred devices, analytical results are needed to understand to understand and control the dynamics of future power systems.

1.2 Purpose of the project

The purpose of this project is to address the aforementioned frequency stability challenging the conventional approach to modeling and control of low-inertia systems and critically reflecting on the notion of system inertia as a stability metric and the role of grid-following and grid-forming control. To this end, this project aims to use reduced-order models for each class of the most common emerging technologies interfaced by power electronics (e.g., wind turbines, photovoltaics, high-voltage DC) to clarify their capabilities (e.g., response time, internal energy storage) and possible contribution to system-level stability. Based on these insights, this project intends to explore a control paradigm that fully leverages the capabilities of power electronics and common energy sources, seamlessly integrates with prevailing operator practices, and reduces system complexity by unifying standard functions of grid-following and grid-forming controls (e.g., primary frequency control, maximum power point tracking) across different technologies. Finally, this project intends to leverage the combination of a common modeling framework and unified system-level control functions to develop analytical stability conditions and clarify the interplay of short-term energy storage elements (e.g., machine inertia, DC link capacitors) and dynamic performance. A particular focus are scalable analytic results that explicitly capture the capabilities of common energy sources, explicitly capture the network structure of the problem, and allow to make predictions for large-scale power systems.

1.3 Objectives

The expected contribution of this project is a unified control and stability analysis framework that integrates grid-forming control of power electronic converters with abstract device-level models of common types of energy sources, such as renewable generation (e.g., wind turbines and photovoltaics), short-term energy storage elements (i.e., machine inertia, capacitive storage), and other common actuators (e.g, HVDC) and allows to bridge the gap between device-level control and system-level stability specifications and performance objectives. In light of the fact that that the loss of inertia is only one aspect of a more fundamental problem this project will develop control schemes that do not rely on emulating rotational inertia. Instead, this project will provide a novel unified framework for control and reliable operation of power systems dominated by power electronic converters. The grid-forming controls to be designed will guarantee transient stability and reliable operation at the level of decentralized primary control and be backwards compatible with conventional machine-based generation and prevailing secondary control architectures. Moreover, the project aims to build on these results to clarify the role of short-term energy storage in power system dominated by power electronics and will provide insight into the trade-off between short-term energy storage (i.e., machine inertia) and system resilience and reliability. A key objective is to reduce the complexity of system-level stability analysis by unifying standard control functions across different technologies and enabling a wide range of technologies to autonomous contribute to ensuring dynamic stability of future power systems.

2 Procedures and methodology

Today's grid has been designed around a few large conventional thermal power plants, and its operation heavily relies on the reduced-order electro-mechanical swing equation model

$$M_l \tfrac{\mathrm{d}}{\mathrm{d}t}\omega_l = P_l - P_{\mathrm{ac},l}, \tag{1a}$$

$$T_{\mathrm{g},l} \tfrac{\mathrm{d}}{\mathrm{d}t} P_l = -P_l - k_{\mathrm{g},l}\omega_l, \tag{1b}$$

where M_l is the inertia coefficient of the l-th generator, ω_l is its rotational frequency, P_l the power generated by the generators turbine (e.g., steam or hydro turbine), $T_{\mathrm{g},l}$ is the turbine/governor time constant, $k_{\mathrm{g},l}$ is the governor gain, and $P_{\mathrm{ac},l}$ denotes the electric AC power flowing out of the machine.

Observe that a large inertia coefficient diminishes the effect of fluctuating load $P_{\mathrm{ac},l}$ on the frequency. In other words, the kinetic energy stored in the rotational mass acts as buffer and instantaneously provides or absorbs power and limits frequency deviation due to power imbalances. Under the assumption that the machine inertia is sufficiently large and homogeneous throughout the grid, that the voltage is robustly regulated, and the machines self-synchronize sufficiently fast, the aggregated swing equation model [22] of the frequency dynamics of a power system is obtained

$$M \tfrac{\mathrm{d}}{\mathrm{d}t}\omega_l = -D\omega_l - P_{\mathrm{demand}} \tag{2}$$

where M is the total inertia (i.e., the sum of the inertia of the individual machines), ω is the system frequency and D aggregates the effects of primary frequency control and load damping. Based on this model it has been observed that low levels of inertia result in large frequency deviations [2, 17, 22].

This has lead to widespread use of the total inertia M as a measure of robustness. However, the total inertia does not correlate well with robustness of the system in some cases [23]. More importantly, the aggregated swing equation model is only a useful abstraction of power system dynamics because of the inherent properties and controls of synchronous machines. In contrast, if the system is largely based on power electronic sources this model becomes invalid and the concept of inertia and total inertia may no longer meaningful or important. For instance, synchronous machines require large amounts of inertia due to the relatively large turbine time constant (on the order of seconds). This turbine time constant is not captured in the aggregated swing equation model. Moreover, power electronic converters with common renewable energy sources (e.g., curtailed photovoltaics or battery storage) can potentially control their power generation on time scales of ten to a hundred milliseconds. Consequently, the concept of inertia may not play an important role in a power system dominated by power electronic converters.

This project challenges the conventional research on transient stability of low-inertia power system which aims to salvage the network level system behavior by partially. Moreover, we challenge the notion of system inertia as a performance metric. The methods in this project are expanding upon ideas and system models that correctly capture the physics of converter-dominated power systems [24, 25] and the grid-forming control [26] that relates the energy stored in power electronic devices to its frequency and thus recovers the core operating principle and self-synchronizing properties of synchronous machines. Because this controller does not rely on measuring the system frequency its performance is not hindered by the associated measurement delays. Moreover, in this project the notion of power system stability is made precise by using stability definitions and performance metrics that do not require the artificial concept of virtual inertia.

The main objective of this project is to use this solid basis to design novel grid-forming control mechanisms tailored to power electronics and different energy sources (i.e., renewable generation and storage) that ensure reliable and efficient operation of tomorrow's power system. To this end, abstract models for each class of the most common renewable sources (e.g., wind turbines, photovoltaics) and short-term energy storage systems need to be developed that capture their uncertainty and operational limits. In contrast to most works on grid-forming control of power converters the controller proposed in [26] allows to make the impact of the dynamics and limitations of the energy source of power electronic converters on grid stability explicit. Thus, combining the power converter model and controller used in [26] with suitable abstract models of different energy sources results in a framework that allows to analyze the interactions of a wide class of actuators, identify suitable control structures, and and asses system stability. Using ideas from singular perturbation theory [26], one obtains a tractable problem that is amenable to ideas from both control of conventional power systems as well as decentralized and distributed control. The main aim of this project is to utilize ideas from these fields to obtain controllers that fully leverage the capabilities of power electronics and common energy sources. Based on this result, one can asses which technologies can make a significant contribution to ensuring stable and reliable operation of power systems dominated by power electronic converters and renewable generation.

In a second step, model reduction techniques can again be applied to reduce the system dynamics, i.e., including power converters, short-term energy storage, and controls to an abstract model that captures the disturbance response of the system purely in terms of its main energy storage elements. Based on this model, we will asses asses how much short-term energy storage and flexibility is needed to ensure system stability. Power electronic converters are a mature technology and the challenge of grid-forming control lies in ensuring stability of large-scale networks of power converters feed by potentially uncertain renewable generation. Because of this, this project mainly aims to obtain analytic results that explicitly capture the network structure of the problem and allow to make predictions for large power systems without relying on simulations or numerical analysis. The analytic results will then be confirmed and illustrated using high-fidelity power systems simulations.

3 Results and discussion

This section will first present the results on reduced-order modeling of renewable generation devices and power electronics. Next, we will present our findings on the unified autonomous real-time control and stability analysis framework. Next, we will clarify the role of short-term energy storage in power system dominated by power electronics using the proposed unified control and discuss insight into the trade-off between short-term energy storage (i.e., machine inertia, converter DC-link capacitor) and frequency stability. Finally, results on integrating the proposed control into standard secondary control frameworks will be presented.

3.1 Modeling of power generation, power conversion, and power transmission

One of the main results of this project is that, from a system level perspective, a wide class of different technologies can be modeled by combining suitable abstract models for power generation, power transmission, and power conversion. In this section, we will use key conventional (e.g., synchronous machines with turbine/governor system) and emerging technologies (e.g., photovoltaics and wind power) to present the modeling framework used for this project. The results crucially hinge on model reduction techniques based on standard time-scale separation arguments applied to emerging technologies. One result of this project is make these time-scale separation arguments rigorous using methods from control theory and robust control [21]. For brevity of the presentation, this section focusses on the application perspective and the reader is referred to [21] for in-depth theoretical results.

3.1.1 Power transmission

Power transmission can be broadly categorized into AC and DC transmission. We will use this terminology in a broader sense that not only covers high voltage AC and DC networks but, e.g., also covers the AC power exchange between the electric machine of a wind turbine and its AC/DC power converter. To that end, the interconnection of three-phase AC nodes with voltage $v_k \in \mathbb{R}^2$ and $v_l \in \mathbb{R}^2$ through a conductor is modeled by the π-line segment depicted in Figure 1. For notional convenience we assign an

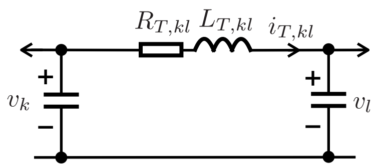

Figure 1: π-line model connecting bus k and l.

index $n \in \mathbb{N}_{[1,N_{T,\text{ac}}]}$ to every AC segment and use $\ell_{T,n}$ and $r_{T,n}$ to denote the inductance and resistance of the segment with index n. The dynamics of the corresponding AC currents $i_T := (i_{T,1}, \dots, i_{T,N_{T,\text{ac}}})$ are given by

$$L_T \tfrac{\mathrm{d}}{\mathrm{d}t} i_T = -Z_T i_T + \mathscr{I}_{\text{ac}}^{\mathsf{T}} v, \tag{3}$$

where $v := (v_1, \dots, v_n) \in \mathbb{R}^{N_{\text{ac}}}$ is the vector of AC bus voltages. Moreover, $L_T := \operatorname{diag}(\{\ell_{T,n}\}_{n=1}^{N_{T,\text{ac}}} \otimes I_2)$, $R_T := \operatorname{diag}(\{r_{T,n}\}_{n=1}^{N_{T,\text{ac}}} \otimes I_2)$, $Z_T := \operatorname{diag}(\{r_{T,n} I_2 + j\omega_0 \ell_{T,n}\}_{n=1}^{N_{T,\text{ac}}})$, and $\mathscr{I}_{\text{ac}} = \mathcal{I}_{\text{ac}} \otimes I_2$ denote the AC network inductance matrix, resistance matrix, impedance matrix, and AC incidence matrix. Moreover, the vector of AC bus current injections is given by $i_o := \mathscr{I}_{\text{ac}} i_T$. In the remainder, we will consider the quasi-steady-state model

$$i_T^s := Z_T^{-1} \mathscr{I}_{\text{ac}}^{\mathsf{T}} v, \qquad i_o^s := \mathscr{I}_{\text{ac}} Z_T^{-1} \mathscr{I}_{\text{ac}}^{\mathsf{T}} v, \tag{4}$$

obtained by neglecting the fast transmission line dynamics (i.e., letting $\frac{\mathrm{d}}{\mathrm{d}t} i_T = \mathbb{0}_{N_{T,\text{ac}}}$).

The approximation $i_o = i_o^s$ is typically justified in conventional power systems due to the pronounced time-scale separation between the dynamics of the transmission lines and the dynamics of synchronous machines. In other words, it is commonly assumed that the error $i_o - i_o^s$ converges to zero very quickly compared to the slow dynamics of synchronous machines. Therefore, the dynamic nature of the transmission lines is typically neglected a priori in transient stability analysis of conventional power systems.

In contrast, the results of this project show that the dynamics of the transmission network have a significant influence on the stability boundaries of converter-dominated power systems [21]. Moreover, contrary to conventional wisdom, sufficiently fast covnergence of the error $i_o - i_o^s$ to zero is, by itself, not sufficient to ensure stability. Instead, both the magnitude of the error $i_o - i_o^s$ (i.e., its overshoot) and convergence rate to zero need to be considered. Both the magnitude of the error over time and its convergence rate can be rigorously quantified using Lyapunov functions and robust control arguments. These bounds can then be used to establish conditions under which the approximation error $i_o - i_o^s$ does not result in instability [21]. We emphasize that requirements on the time-scale separation can typically only be rigorously quantified after obtaining suitable stability certificates for the overall power system model without network dynamics and then enforcing a suitable time-scale separation through the converter control [21].

Using the quasi-steady-state network model and defining the phase angle $\theta_k = \angle v_k$ and magnitude $V_k = \|v_k\|$ for the voltage at bus k results in the well known AC power flow equations [27]

$$P_k = \sum\nolimits_{l=1}^{N_{\text{ac}}} V_k V_l \left(g_{kl} \cos(\theta_k - \theta_l) + b_{kl} \sin(\theta_k - \theta_l) \right), \tag{5a}$$

$$Q_k = \sum\nolimits_{l=1}^{N_{\text{ac}}} V_k V_l \left(g_{kl} \sin(\theta_k - \theta_l) - b_{kl} \cos(\theta_k - \theta_l) \right), \tag{5b}$$

where $g_{kl} = \frac{r_{T,kl}}{\omega_0^2 \ell_{T,kl}^2 + r_{T,kl}^2}$ and $b_{kl} = \frac{\omega_0 \ell_{T,kl}}{\omega_0^2 \ell_{T,kl}^2 + r_{T,kl}^2}$ denote the conductance and susceptance of the line connecting the bus k and l. Moreover, the conductance and susceptance of the AC segment are the edge weights of the AC graph. Next, we define the angle $\delta_{kl} \coloneqq \arctan(\frac{\omega_0 \ell_{T,kl}}{r_{T,kl}})$ and recall that $\sin(\delta_{kl}) = \frac{\omega_0 \ell_{T,kl}}{\sqrt{\omega_0^2 \ell_{T,kl}^2 + r_{R,kl}^2}}$ and $\cos(\delta_{kl}) = \frac{r_{T,kl}}{\sqrt{\omega_0^2 \ell_{T,kl}^2 + r_{T,kl}^2}}$. Using fundamental trigonometric manipulations, power flow equations (5) are equivalent to

$$P_k = \sum\nolimits_{l=1}^{N_{\text{ac}}} V_k V_l \mathfrak{c}_{kl} \cos(\theta_k - \theta_l - \delta_{kl}), \tag{6a}$$

$$Q_k = \sum\nolimits_{l=1}^{N_{\text{ac}}} V_k V_l \mathfrak{c}_{kl} \sin(\theta_k - \theta_l - \delta_{kl}), \tag{6b}$$

where $\mathfrak{c}_{kl} \coloneqq \sqrt{g_{kl}^2 + b_{kl}^2} = \frac{1}{\sqrt{\omega_0^2 \ell_{T,kl}^2 + r_{R,kl}^2}}$.

Moreover, the interconnection of DC nodes with voltage $v_{\text{dc},k}$ and $v_{\text{dc},l}$ through a conductor is modeled by the single-phase π-line segment depicted in Figure 2 and conductance

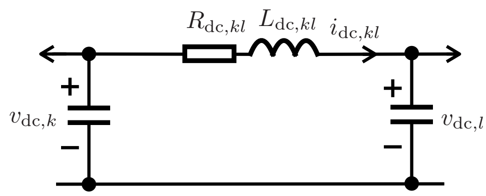

Figure 2: DC line connecting bus k and l.

$$g_{\text{dc},kl} \coloneqq \frac{1}{r_{\text{dc},kl}}, \tag{7}$$

where $r_{\text{dc},kl}$ is the resistance of the DC π-line segment connecting node k and l. For notional convenience we assign an index $n \in \mathbb{N}_{[1,N_{T,\text{dc}}]}$ to every DC segment and use $\ell_{\text{dc},n}$ and $r_{\text{dc},n}$ to denote the inductance and resistance of the segment with index n. The dynamics of the corresponding DC currents $i_{T,\text{dc}} \coloneqq (i_{T,\text{dc},1}, \ldots, i_{T,\text{dc},N_{T,\text{dc}}})$ are given by

$$L_{\text{dc}} \tfrac{\mathrm{d}}{\mathrm{d}t} i_{T,\text{dc}} = -R_{\text{dc}} i_{T,\text{dc}} + B_{\text{dc}}^{\mathsf{T}} v_{\text{dc}}, \tag{8}$$

where $v_{\text{dc}} \coloneqq (v_{\text{dc},1}, \ldots, v_{\text{dc},n}) \in \mathbb{R}^{N_{\text{dc}}}$ is the vector of DC bus voltages, $L_{\text{dc}} \coloneqq \operatorname{diag}(\{\ell_{\text{dc},n}\}_{n=1}^{N_{T,\text{dc}}})$ and $R_{\text{dc}} \coloneqq \operatorname{diag}(\{r_{\text{dc},n}\}_{n=1}^{N_{T,\text{dc}}})$ denote the DC network inductance and resistance matrix. Moreover, the vector of DC bus current injections is given by $i_{\text{dc}} \coloneqq \mathcal{I}_{\text{dc}} i_{T,\text{dc}}$. Neglecting the DC π-line dynamics (i.e., letting $\frac{\mathrm{d}}{\mathrm{d}t} i_{T,\text{dc}} = \mathbb{0}_{N_{T,\text{dc}}}$), the DC currents are given by

$$i_{T,\text{dc}}^s \coloneqq R_{\text{dc}}^{-1} B_{\text{dc}}^{\mathsf{T}} v_{\text{dc}}, \qquad i_{o,\text{dc}}^s \coloneqq \underbrace{\mathcal{I}_{\text{dc}} R_{\text{dc}}^{-1} B_{\text{dc}}^{\mathsf{T}}}_{=:L_{\text{dc}}} v_{\text{dc}}. \tag{9}$$

The assumption that the DC π-line dynamics can again be validated analytically using the methods developed in [21].

3.1.2 Power conversion

This project investigated two broad classes of power conversion devices. Voltage source converters typically used to interfaced renewable generation and high voltage DC transmission, and electric machines commonly used in conventional generation and wind turbines.

Voltage source converters: The prevalent converter architecture for grid-forming DC/AC converters is the two-level voltage source converter (VSC) that consists of a DC source, a DC-link capacitor, a switching stage, and an output filter as shown in Figure 3. Moreover, we consider a standard grid-forming converter control architecture that consists of a reference model providing a reference for the terminal voltage v_f which is tracked by cascaded current and voltage proportional-integral (PI) controllers. The output of the cascaded inner controls determines the modulation signal that controls the switches [28].

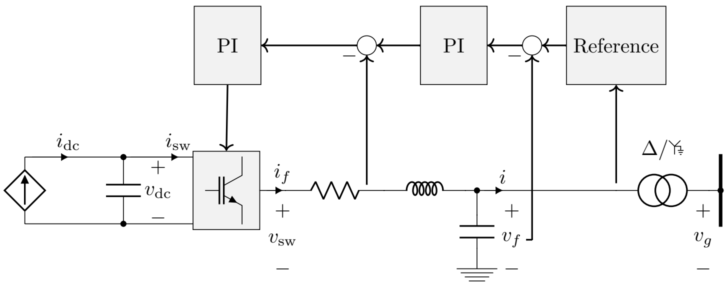

Figure 3: Two-level DC/AC voltage source converter with a reference model for the terminal voltage and cascaded inner current and voltage controllers. In medium and high-voltage networks two-level DC/AC converters are typically connected to the grid via a delta-wye transformer.

Commonly a continuous-time average model is used to analyze networks of power converters. The use of the averaged model is justified because the pulse-width-modulation (PWM) carrier frequency (≈ 10 kHz) is significantly larger that the AC signals after the conversion (e.g., 50 Hz). Using $v_{\text{sw}} \in \mathbb{R}^2$ denotes the modulated voltage, $i_{sw} \in \mathbb{R}$ denotes the current flowing out of the DC-link capacitor into the switches, and i_f denotes the output filter current [26]. Moreover, the DC terminal current $i_{\text{dc}} \in \mathbb{R}$ is charging the DC-link capacitor with capacitance C_{dc} and the AC terminal circuit is a low-pass RLC filter with resistance $r_f \in \mathbb{R}_{>0}$, inductance $\ell_f \in \mathbb{R}_{>0}$, capacitance $c_f \in \mathbb{R}_{>0}$, and conductance $g_f \in \mathbb{R}_{>0}$. Considering the DC-link capacitor dynamics and RLC output filter dynamics, we obtain the averaged converter model

$$c_{\text{dc}} \tfrac{\mathrm{d}}{\mathrm{d}t} v_{\text{dc}} = -g_{\text{dc}} v_{\text{dc}} + i_{\text{dc}} - i_{\text{sw}} \tag{10a}$$

$$\ell_f \tfrac{\mathrm{d}}{\mathrm{d}t} i_f = -\underbrace{(r_f I_2 + j\omega_0 \ell_f)}_{=:Z_f} i_f - v_f + v_{\text{sw}} \tag{10b}$$

$$c_f \tfrac{\mathrm{d}}{\mathrm{d}t} v_f = -\underbrace{(g_f I_2 + j\omega_0 c_f)}_{=:Y_f} v_f + i_f - i, \tag{10c}$$

where, $v_{\text{dc}} \in \mathbb{R}_{\geq 0}$ is the DC voltage and $i \in \mathbb{R}^2$ denotes the current flowing into the grid [21]. This averaged model of the DC/AC converter is presented on Figure 4. A standard assumption in the literature is that the RLC output filter dynamics are controlled through a cascaded current and voltage controller. In this setup, the voltage reference $v_f^\star \in \mathbb{R}^2$ is tracked by the following two-degree of freedom proportional-integral controller.

$$\tfrac{\mathrm{d}}{\mathrm{d}t} \zeta_v := v_f - v_f^\star, \tag{11a}$$

$$i_f^\star := Y_f v_f + i - K_{p,v_f}(v_f - v_f^\star) - K_{i,v_f} \zeta_v, \tag{11b}$$

where the term $Y_f v_k$ compensates the filter admittance losses, $\zeta_v \in \mathbb{R}^2$ is an integrator state, and $i_f^\star \in \mathbb{R}^2$

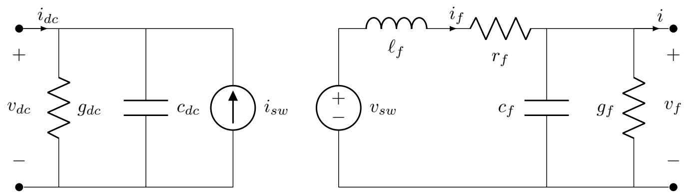

Figure 4: Averaged model of the DC/AC converter.

is the current reference tracked by a two-degree of freedom current PI controller

$$\tfrac{\mathrm{d}}{\mathrm{d}t}\zeta_f := i_f - i_f^\star \tag{12a}$$

$$m := \frac{1}{v_{\text{dc}}}\left(Z_f i_f + v_f - K_{p,i_f}(i_f - i_f^\star) - K_{i,i_f}\zeta_f\right), \tag{12b}$$

where the term $Z_f i_f$ compensates the filter impedance losses, $\zeta_f \in \mathbb{R}^2$ is an integrator state, and $m \in \mathbb{R}^2$ is the averaged modulation signal driving the converter switches.

In analysis of multi-converter systems it is commonly assumed that the dynamics of the controlled current and voltage are fast and negligible, i.e., that the converter perfectly tracks the voltage reference $v_f^\star$. This time-scale separation argument can be made rigorous by quantifying the peak value and convergence rate of the resulting modeling error through Lyapunov functions [21].

For the purpose of this report, we assume perfect voltage tracking and neglect the inner control loops. Moreover, assuming that the voltage reference of the converter is given in polar coordinates with angle $\theta \in \mathbb{R}$ and magnitude $V \in \mathbb{R}$, we obtain $\angle v_f = \theta$ and $\|v_f\| = V$. Next, using the DC-link capacitor voltage v_{dc} and assuming that the output filter losses are negligible, we obtain the simplified model

$$C_{\text{dc}}\tfrac{\mathrm{d}}{\mathrm{d}t}v_{\text{dc}} = i_{\text{dc}} - v_{\text{dc}}^{-1}P, \tag{13}$$

where P is the power injected into the AC grid given by (5) and $i_{\text{dc}} \in \mathbb{R}$ is the current supplied on the DC terminal, either by power generation, storage, or through a DC network . In summary, the model (13) captures the input-output behavior of the converter as seen from its AC and DC terminals, but neglects the controlled internal RLC filter dynamics. Our results show that a suitable time-scale separation between the converter filter dynamics, power network dynamics, and controls can be enforced through the converter control parameters [21]. In particular, the framework developed in [21] provides explicit bounds on the control gains that show that the controlled RLC filter dynamics need to be faster than those of the transmission lines, which in turn need to be faster than those of the outer controls that provide the voltage reference for (11).

Similar arguments have been used in this project to develop reduced order models of modular multi-level converters commonly used in HVDC applications [29]. Control of MMCs is a challenging problem that requires an intricate internal control structure that contains energy balancing controls which stabilize the internal dynamics of the MMC [30, 31]. Using an averaged model for each arm (i.e., averaging the voltage of the inserted sub modules) and assuming that the internal controls are well tuned (e.g., using a method such as [31]) a macroscopic model that captures the main salient features of the dynamics of the MMC can be obtained that is of the same form as (13) but uses the MMC's internal energy instead of the converter DC voltage. Moreover, the MMC terminals can be modeled as a controllable AC and DC voltage source [29].

Generalized three-phase machine: The generalized machine is shown in Figure 5 and consists of a rotor with inertia constant M that is driven by the mechanical torque τ_m and the electrical torque τ_e extracted from the rotor, through the machine windings. The electrical part consists of a stator that is connected to the grid and a rotor with two windings [1] that are each controlled by a rotor voltage. The rotor

[1] The generalized three phase machine has three rotor windings, but assuming a balanced system the machine can be equivalently represented using two windings in dq coordinates.

voltages can be used to induce a rotating field in the rotor, resulting in a doubly-fed induction machine whose slip speed can be controlled. In contrast, if one of the two rotor voltages is set to zero, we recover the model of a synchronous machine [24].

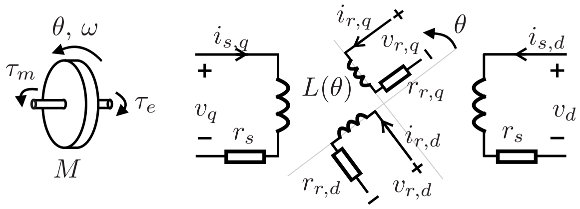

Figure 5: Mechanical and electrical components of a doubly fed machine.

The current vector $i = (i_s, i_r) \in \mathbb{R}^4$ aggregates the stator currents $i_s = (i_d, i_q) \in \mathbb{R}^2$ and rotor currents $i_r = (i_d, i_q) \in \mathbb{R}^2$. Moreover, voltage vector $v = (v_s, v_r) \in \mathbb{R}^4$ collects the stator $v_s \in \mathbb{R}^2$ and rotor voltages $v_r \in \mathbb{R}^2$. The rotational speed is denoted with $\omega_m \in \mathbb{R}_{>0}$ and its nominal value is given by $\omega_m^\star \in \mathbb{R}_{>0}$. Next, $\theta_m \in \mathbb{R}$ denotes the angular displacement of the rotor, $\omega_r \in \mathbb{R}_{>0}$ is the rotational frequency of rotor excitation voltage and $\omega_r^\star \in \mathbb{R}_{>0}$ is used to denote its nominal value. Lastly, $\tau_e \in \mathbb{R}$ is the electrical torque acting on the rotor and stator, and induced voltage is denoted with $v_{\text{ind}} = (v_{\text{ind},s}, v_{\text{ind},r}) \in \mathbb{R}^4$, where $v_{ind,s} \in \mathbb{R}^2$ and $v_{ind,s} \in \mathbb{R}^2$ are the voltages induced on the stator and rotor sides respectively. Finally, the generalized machine model, in the rotating frame, is given by

$$\tfrac{\mathrm{d}}{\mathrm{d}t}\theta_m = \omega_m - \omega_m^\star \tag{14a}$$
$$m_m \tfrac{\mathrm{d}}{\mathrm{d}t}\omega_m = -d_m\omega_m - \tau_e + \tau_m \tag{14b}$$
$$L(\theta_m)\tfrac{\mathrm{d}}{\mathrm{d}t} i = -Z(\theta_m) i + v - v_{ind}. \tag{14c}$$

where the rotor variables are expressed in a rotating frame with frequency $\omega_r^\star$ and the stator variables are in a rotating frame with frequency ω_0. The machine is actuated by the voltage $v_r \in \mathbb{R}^2$ across the excitation winding of the generator and the mechanical torque $\tau_m \in \mathbb{R}$ applied to the rotor. The inertia coefficient and friction coefficient of the rotor are denoted by $m_m \in \mathbb{R}_{>0}$ and $d_m \in \mathbb{R}_{>0}$; $r_s \in \mathbb{R}_{>0}$ and $r_r \in \mathbb{R}_{>0}$ denote the stator and rotor resistance. Finally, the inductance matrix $L(\theta_m) : \mathbb{R} \to \mathbb{R}^{4\times 4}$ models the inductive coupling of the rotor and stator and is defined by

$$L(\theta_m) = \begin{bmatrix} I_2 \ell_s & \ell_m \mathcal{R}(\theta_m) \\ \ell_m \mathcal{R}(\theta_m)^\mathsf{T} & I_2 \ell_r \end{bmatrix},$$

where $\ell_s \in \mathbb{R}_{>0}$, $\ell_r \in \mathbb{R}_{>0}$, $\ell_m \in \mathbb{R}_{>0}$, and $\mathcal{R}(\theta_m) \in \mathbb{R}^{2\times 2}$ denote the stator inductance, rotor inductance, mutual inductance, and 2D rotation matrix. Based on this definition of the inductance matrix, the impedance matrix $Z(\theta_m) \in \mathbb{R}^{4\times 4}$ is defined as

$$Z(\theta_m) = \begin{bmatrix} Z_s & j\mathcal{R}(\theta_m)\ell_m\omega_r^\star \\ j\mathcal{R}(\theta_m)^\mathsf{T}\ell_m\omega_0 & Z_r \end{bmatrix}, \tag{15}$$

where $\omega_0 \in \mathbb{R}_{>0}$ is the nominal grid frequency, $Z_s = I_2 r_s + j\omega_0\ell_s \in \mathbb{R}^{2\times 2}$ is the stator impedance matrix, and $Z_r = I_2 r_m + j\omega_r^\star \ell_r \in \mathbb{R}^{2\times 2}$ is the rotor impedance matrix. We emphasize that for a grid-connected machine in steady state it needs holds that $\omega_0 = \omega_m^\star + \omega_r^\star$.

Moreover, defining $\jmath = \operatorname{diag}(j, \mathbb{0}_2)$, the electrical torque acting on the rotor is given by

$$\tau_e = \tfrac{1}{2} i^\top \big(L(\theta_m)\jmath + \jmath^\top L(\theta_m)\big) i = \ell_m i_r^\mathsf{T} j \mathcal{R}(\theta_m)^\mathsf{T} i_s, \tag{16}$$

and the voltage $v_{\text{ind}} \in \mathbb{R}^4$ induced in the machine windings due to the rotation of the machine is given by

$$v_{\text{ind}} = \omega_m \big(L(\theta_m)\jmath^\top + \jmath L(\theta_m)\big) i = \omega_m \begin{bmatrix} \mathbb{0}_{2\times 2} & j\mathcal{R}(\theta_m)\ell_m \\ (j\mathcal{R}(\theta_m))^\mathsf{T}\ell_m & \mathbb{0}_{2\times 2} \end{bmatrix} i. \tag{17}$$

In order to obtain a reduced model that clarifies the interaction of the main energy storage elements and power flows, we assume that the voltage at the stator terminal (i.e., the grid voltage) is of the form $v_s = \mathcal{R}(\theta_s)\begin{bmatrix}V_s & 0\end{bmatrix}^\mathsf{T} = r(\theta_s)V_s$ and the voltage applied to the rotor (i.e., the excitation voltage) is of the form $v_r = \mathcal{R}(\theta_r)\begin{bmatrix}V_r & 0\end{bmatrix}^\mathsf{T} = r(\theta_r)V_r$, where θ_s is the stator voltage phase angle relative to the rotating frame at ω_0 and θ_r is the rotor voltage phase angle relative to the coordinate frame rotating at $\omega_r^\star$ (i.e., $\omega_r^\star = 0$ for a synchronous machine).

Substituting (17), into (14c) results in

$$\ell_s \tfrac{\mathrm{d}}{\mathrm{d}t} i_s + \ell_m \mathcal{R}(\theta_m) \tfrac{\mathrm{d}}{\mathrm{d}t} i_r = -Z_s i_s - j\mathcal{R}(\theta_m)\ell_m(\omega_r^\star + \omega_m) i_r + v_s \tag{18a}$$

$$\ell_m \mathcal{R}(\theta_m)^\mathsf{T} \tfrac{\mathrm{d}}{\mathrm{d}t} i_s + \ell_r \tfrac{\mathrm{d}}{\mathrm{d}t} i_r = -Z_r i_r - j\mathcal{R}(\theta_m)^\mathsf{T} \ell_m(\omega_0 - \omega_m) i_s + v_r. \tag{18b}$$

Next, setting both derivatives ($\tfrac{\mathrm{d}}{\mathrm{d}t} i_s \overset{!}{=} 0$, $\tfrac{\mathrm{d}}{\mathrm{d}t} i_r \overset{!}{=} 0$) results in

$$\begin{bmatrix} Z_s & j\mathcal{R}(\theta_m)\ell_m(\omega_r^\star + \omega_m) i_r \\ j\mathcal{R}(\theta_m)^\mathsf{T} \ell_m(\omega_0 - \omega_m) & Z_r \end{bmatrix} \begin{bmatrix} i_s \\ i_r \end{bmatrix} = \begin{bmatrix} r(\theta_s)V_s \\ r(\theta_r)V_r \end{bmatrix}. \tag{19}$$

A straightforward calculation reveals that (19) is equivalent to

$$\begin{bmatrix} \bar{Z}_s & 0 \\ 0 & \bar{Z}_r \end{bmatrix} \begin{bmatrix} i_s \\ i_r \end{bmatrix} = \begin{bmatrix} r(\theta_s)V_s \\ r(\theta_r)V_r \end{bmatrix} - \begin{bmatrix} V_{e,s} r(\theta_m + \theta_r - \delta_s) \\ V_{e,r} r(\theta_s - \theta_m - \delta_r) \end{bmatrix}. \tag{20}$$

where $\delta_s = -\frac{\pi}{2} + \arctan \frac{\omega_0 \ell_s}{r_s}$, $\delta_r = -\frac{\pi}{2} + \arctan \frac{\omega_r^\star \ell_r}{r_r}$ are angles modeling the stator and rotor losses[2]. Moreover, the equivalent voltage magnitudes are given by

$$V_{e,s} := V_r \frac{\ell_m(\omega_m + \omega_r^\star)}{\sqrt{\omega_0^2 \ell_s^2 + r_s^2}}, \tag{21a}$$

$$V_{e,r} := V_s \frac{\ell_m(\omega_0 - \omega_m)}{\sqrt{\omega_r^{\star 2} \ell_r^2 + r_r^2}}, \tag{21b}$$

and the equivalent impedances are given by

$$\bar{Z}_s := Z_s + \ell_m^2(\omega_m + \omega_r^\star)(\omega_0 - \omega_m) Z_r^{-1} = \bar{r}_s I_2 + j\omega_0 \bar{\ell}_s, \tag{22a}$$

$$\bar{Z}_r := Z_r + \ell_m^2(\omega_m + \omega_r^\star)(\omega_0 - \omega_m) Z_s^{-1} = \bar{r}_r I_2 + j\omega_r^\star \bar{\ell}_r. \tag{22b}$$

We emphasize that the equivalent resistances and inductances $\bar{r}_s$, $\bar{r}_r$, $\bar{\ell}_s$, and $\bar{\ell}_r$ depend on ω_m and they are given with the following expressions

$$\bar{r}_s = r_s + r_r \frac{\ell_m(\omega_m + \omega_r^\star)}{\|Z_r\|} \frac{\ell_m(\omega_0 + \omega_m)}{\|Z_r\|}, \qquad \bar{\ell}_s = \ell_s - \ell_r \frac{\omega_r^\star}{\omega_0} \frac{\ell_m(\omega_m + \omega_r^\star)}{\|Z_r\|} \frac{\ell_m(\omega_0 + \omega_m)}{\|Z_r\|}, \tag{23a}$$

$$\bar{r}_r = r_r + r_s \frac{\ell_m(\omega_m + \omega_r^\star)}{\|Z_s\|} \frac{\ell_m(\omega_0 + \omega_m)}{\|Z_s\|}, \qquad \bar{\ell}_r = \ell_r + \ell_s \frac{\omega_0}{\omega_r^\star} \frac{\ell_m(\omega_m + \omega_r^\star)}{\|Z_s\|} \frac{\ell_m(\omega_0 + \omega_m)}{\|Z_s\|}. \tag{23b}$$

Moreover, the power flowing out of the stator and rotor can be computed based on the equivalent circuit, the line impedance given by (22), and the AC power flow equations (5). For example, for a doubly-fed induction machine, the stator voltage v_s is the grid voltage at the point of coupling, and v_r is generated by a DC/AC power converter. Next, the electrical torque τ_e can be rewritten in terms of the power injected to the grid and power losses in the rotor and stator

$$\tau_e = \frac{\frac{1}{2}(P_{\text{losses}} - P_e)}{(\omega_m - \frac{1}{2}\omega_m^\star)}, \tag{24}$$

where $P_{\text{loss}} = i_s^\mathsf{T} Z_s i_s + i_r^\mathsf{T} Z_r i_r$ and $P_e = v_s^\mathsf{T} i_s + v_r^\mathsf{T} i_r = P_s + P_r$ is the electric power flowing out of the machine (i.e., into the grid and the rotor side converter).

[2] If there are no losses in either stator (rotor) it holds that $\delta_s = 0$ ($\delta_r = 0$).

Synchronous machine: The model of a synchronous machine is directly obtained from the generalized three-phase machine model (14) by taking $\omega_r = \omega_r^\star = 0$ and $\theta_r = 0$. In other words, an excitation system supplies the voltage for the d-axis excitation winding and the q-axis rotor winding acts as a damper winding. Moreover, the stator winding is directly connected to the grid, i.e., v_s is the grid voltage. If the machine is synchronous with the nominal grid frequency (i.e., $\omega_m = \omega_0$), the second line of (20) becomes $r_r i_{r,d} = V_r$, i.e., the excitation system only supplies the rotor losses and the power flowing from the excitation system into the rotor and the losses in the stator and rotor is negligible. This approximation is typically justified during nominal operation, when ω_m deviates at most one percent from ω_0. Based on these simplifications, the following reduced-order model of a synchronous machine is obtained

$$\tfrac{\mathrm{d}}{\mathrm{d}t}\theta_m = \omega_m \tag{25a}$$

$$m_m \tfrac{\mathrm{d}}{\mathrm{d}t}\omega_m = -d_m\omega_m + \tau_m - \tau_e, \tag{25b}$$

where $\tau_m \in \mathbb{R}_{\geq 0}$ is the mechanical power input and $\tau_e \in \mathbb{R}$ is the electrical torque that can be obtained from (24), the power flow equations (5). Moreover, we assume a standard proportional-integral (PI) AVR is used to control the voltage magnitude at the machine terminal.

Doubly-fed machine: Next, we investigate a doubly-fed machine, i.e., the generalized machine with a controllable AC voltage source attached to the rotor windings that can induce a rotating voltage in the stator. In particular, if the rotor side voltage source induces a rotating field at a constant frequency $\omega_r^\star$ and the stator is connected to a grid with frequency ω_0, the machine will synchronize to a speed of $\omega_m^\star = \omega_0 - \omega_r^\star$. In wind power applications this additional degree of freedom is typically used to control the stator and rotor currents and perform grid-following maximum power point tracking control. To develop a of the power flows in the equivalent stator and rotor circuit are of a doubly-fed machine we introduce the effective machine AC voltage angle $\theta_v := \theta_m + \theta_r$ (i.e., the angle of the voltage behind the stator) as well as the angles $\alpha_s := \bar{\delta}_s - \delta_s$ and $\alpha_r := \bar{\delta}_r - \delta_r$, $\bar{\delta}_s := \arctan(\frac{\omega_0 \bar{\ell}_s}{\bar{r}_s})$, and $\bar{\delta}_r := \arctan(\frac{\omega_r^\star \bar{\ell}_r}{\bar{r}_r})$. The power injection through the stator and rotor circuit are given by the standard power flow equations

$$P_s = V_s V_{e,s} \mathfrak{c}_s \cos(\theta_s - \theta_v - \alpha_s), \quad Q_s = V_s V_{e,s} \mathfrak{c}_s \sin(\theta_s - \theta_v - \alpha_s), \tag{26a}$$

$$P_r = V_r V_{e,r} \mathfrak{c}_r \cos(\theta_v - \theta_s - \alpha_r), \quad Q_r = V_r V_{e,s} \mathfrak{c}_r \sin(\theta_v - \theta_s - \alpha_r). \tag{26b}$$

where $\mathfrak{c}_s := \frac{1}{\sqrt{\omega_0^2 \bar{\ell}_s + \bar{r}_s^2}}$ and and $\mathfrak{c}_r := \frac{1}{\sqrt{\omega_r^{\star 2} \bar{\ell}_r + \bar{r}_r^2}}$. Combining this power flow model with the generalized machine model and assuming a power converter applies an AC voltage to the rotor with angle θ_r with control input $\frac{\mathrm{d}}{\mathrm{d}t}\theta_r = \omega_r$, we obtain the reduced order dynamics of the effective AC voltage frequency $\omega_v = \omega_m + \omega_r$ and effective AC voltage angle θ_v.

$$\tfrac{\mathrm{d}}{\mathrm{d}t}\theta_v = \omega_v - \omega_0, \tag{27a}$$

$$m_m \tfrac{\mathrm{d}}{\mathrm{d}t}\omega_v = -d_m(\omega_v - \omega_r) - \tau_e + \tau_m - m_m \tfrac{\mathrm{d}}{\mathrm{d}t}\omega_r. \tag{27b}$$

It can be seen that this model is almost in the form of a synchronous machine. Given a (constant) effective machine frequency set-point $\omega_v^\star \in \mathbb{R}_{\geq 0}$ we design a grid-forming controller

$$\omega_r = \omega_r^\star - k_v(\omega_v^\star - \omega_v) \tag{28}$$

that leverages the degrees of freedom of the doubly-fed machine and simplifies the analysis. Substituting (28) into (27b) results in

$$(m_m + k_v)\tfrac{\mathrm{d}}{\mathrm{d}t}\omega_v = -d_m(1 + k_v)(\omega_v - \omega_v^\star) - d_m\omega_m^\star - \tau_e + \tau_m, \tag{29}$$

i.e., the dynamics of the doubly-fed machine are now in the same form of synchronous machine dynamics, but the difference between the effective AC frequency and rotor speed, as well as the inertia and damping can be modified through $\omega_r^\star$ and the control gain $k_v \in \mathbb{R}_{\geq 0}$. Moreover, for steady-state operation at $\omega_v = \omega_v^\star$, the mechanical steady-state losses $d_m\omega_m^\star$ need to be provided either through the mechanical or electrical torque. However, the power converters of doubly-fed induction machines that are used in, e.g., wind power applications are only sized to provide a limited amount of rotor speed control and reactive power control and rated for up to 20% of the overall machine power. This limits the overall controllability of the doubly-fed machines and the ability to provide grid-forming functions. In the remainder of the report we will therefore focus on wind turbines with permanent magnet synchronous machines interfaced through full-scale back-to-back power converters.

3.1.3 Power Generation

The main result of this project is that, in the context of grid-forming control design, the key dynamics and limitations of power generation technologies ranging from fully dispatchable power sources such as conventional thermal generation and fuel cells, to renewable sources such as photovoltaics and wind power, can be modeled through two abstract power generation models that model mechanical power (e.g., thermal generation, wind turbines) and DC power sources (e.g., photovoltaics, fuel cells).

Mechanical power sources: We first review the basic linear model for steam and hydro turbines and typical speed governing systems that are applicable for system-level stability studies. In particular, the turbine and speed governor dynamics are modeled by proportional speed droop control and first order turbine dynamics [27]

$$T_T \tfrac{\mathrm{d}}{\mathrm{d}t} \tau_T = -\tau_T + \tau_T^\star + K_D(\omega_m^\star - \omega_m), \tag{30}$$

where $T_T \in \mathbb{R}_{>0}$ is the combined turbine governor time-constant, $K_D \in \mathbb{R}_{\geq 0}$ is the speed droop gain, τ_T is the turbine torque, ω_m is its rotational speed, and ω_0 denotes the nominal system frequency. The torque τ_T can vary between zero and the maximum torque $\bar{\tau}_T$ or rated power of the turbine. Therefore, given a gain K_D, that is typically prescribed by grid-codes or market mechanisms, the operating point $\tau_T^\star$ is typically chosen such that $0 \leq \tau_T^\star + K_D(\omega_m^\star - \omega_m) \leq \bar{\tau}_T$ holds for frequencies ω_m in the normal operating range of a power system (i.e., $50\mathrm{Hz} \pm 250\mathrm{mHz}$ in Europe). The time constant T_T is typically the range of $1\mathrm{s}$ for small-scale hydro turbines to $11\mathrm{s}$ for large-scale nuclear or fossil-fuel based generation [32]. While the model (30) is widely used in the literature, it should be noted that it is a simplified and unified abstraction of different technologies. In particular, for steam turbines more detailed models are usually given by transfer functions with two poles, while more detailed models of hydro turbines consist of a transfer function with a pole and a zero [32]. Thus, increasing the model fidelity will result in different model structures for different generation technologies. To obtain a model that is tractable for system-level analysis of large-scale systems, we restrict our attention to the simplified model (30).

Another key mechanical power source are wind turbines. Wind turbines operated with curtailment are widely considered as a promising source of active power control [33, 34, 35, 36, 37]. In fact, wind turbines have been used for active power control by several TSOs in countries such as Spain, Denmark and Ireland, where new wind plants are required to have a number of active power control capabilities in order to regulate grid frequency [36, 37]. However, these works considered wind turbines in isolation and typically consider the grid-following case, i.e., the wind turbine measure the grid frequency and responds to changes in grid-frequency by changing its active power injection. In this section, we will model the aerodynamic and mechanical part of the wind turbine that together form the part of the wind turbine that generates power. The power conversion elements (e.g., the generalized three-phase machine and voltage source converter) discussed in the previous section can be combined with this model to obtain the complete model for several different wind turbine architectures (i.e., using a doubly-fed induction machine or full scale back to back converters). Two different operating regimes have to be differentiated. In the region below the rated wind speed, the power generated from wind is given by the wind speed relative to rotational speed of the blades. In contrast, in the full load region wind speeds are high enough to drive the wind turbine at its rated speed and the power generation is reduced by adjusting the blade pitch to avoid overspeeding.

The blades are actuated with pitch motors which are often modeled as low-pass filters with a cut-off frequency of the order of $1\mathrm{Hz}$ subject to constraints on the pitch angle [33]. This results in the model for the torque τ_w on the rotor generated by the wind [35]

$$T_\beta \tfrac{\mathrm{d}}{\mathrm{d}t} \beta = -\beta + \beta^\star, \tag{31a}$$

$$\tau_w = \frac{1}{2} \rho \pi R^3 v^2 C_q(\lambda, \beta), \tag{31b}$$

where β is the blade pitch angle, T_β is the time-constant modeling the response time of the pitch motors, R is the radius of the rotor disk, ρ denotes the air density, and v the wind speed. The aerodynamic torque coefficient $C_q(\lambda, \beta) \in \mathbb{R}_{\geq 0}$ depends on the tip speed ratio $\lambda_w = \frac{\omega_m R}{v}$, where ω_m is the rotational speed of the rotor, and models how much of the theoretical maximum torque $\frac{1}{2}\rho\pi R^3 v^2$ can be generated from the wind. The coefficient C_q can be approximated through analytic functions. Figure 6 shows typical values of C_q for a 5 MW wind turbine obtained using the model and parameters for C_q taken from [38]. The model (31) is an approximation based on stationary flows around the blades that is typically used

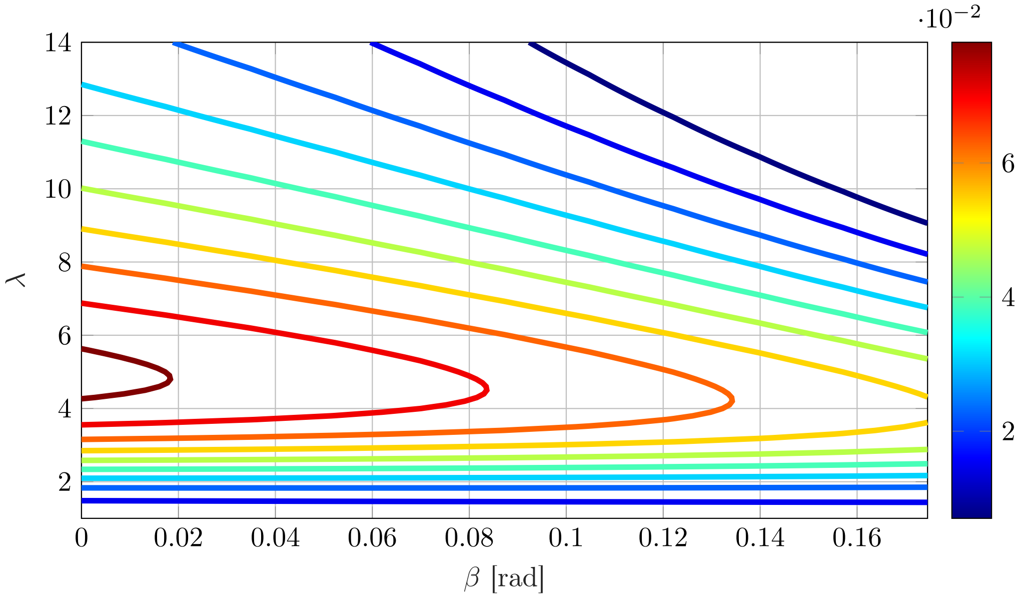

Figure 6: Values of $C_q(\lambda, \beta)$ for a 5 MW wind turbine.

in control design. In the operating region below the rated wind speed the pitch angle is typically set to extract maximum power (i.e., $\beta = 0$). In this regime, operating above the maximum power point, i.e., $\lambda > \lambda_{\text{MPP}}$, an increase in mechanical load on the turbine will result in a decrease of the rotor speed ω_m and lower tip speed ratio and hence increased power generation (see Figure 6). In other words,

$$\frac{\partial}{\partial \omega_m} C_q(\lambda, \beta)\bigg|_{\beta=0} < 0 \quad \forall \lambda > \lambda_{\text{MPP}} \tag{32}$$

On the other hand, in the full load region the blade pitch can be used to curtail the power generation and increase it when needed, in this case T_β has to be considered. To obtain a simplified model, we introduce operating region dependent time constant, i.e., $T_w(v) = T_\beta$ at above rated wind speed and $T_w(v)$ very small (approximating dynamic inflow effects) below the rated windspeed and linearize the resulting dynamics to obtain

$$T_w(v) \tfrac{\mathrm{d}}{\mathrm{d}t} \tau_w = -\tau_w - k_g(\omega_m - \omega^\star) + k_\beta(\beta - \beta_0), \tag{33}$$

where $\beta_0 \in \mathbb{R}_{[0, \beta_{\max}]}$ is the pitch angle at the current operating point and $\beta \in \mathbb{R}_{[-\beta_0, \beta_{\max} + \beta_0]}$ is a control input. Moreover, k_g and k_β are operating point dependent sensitivities of the wind turbine torque with respect to rotor speed and pitch angle changes. We conclude that the electromechanical part of a wind turbine admits a reduced-order model that is equivalent to that of conventional generation.

It can be seen that the wind turbine power production can be curtailed either through increasing the pitch angle (maximum power generation is achieved for $\beta = 0$) or increasing the rotor speed beyond the speed at the maximum power point. From a system-level point of view, the option to curtail the power production by increasing the rotor speed is preferable because it results in significant kinetic energy stored in the wind turbine rotor that can be released into the grid as needed. In contrast, curtailing power production only through the pitch angle simpy decreases the power generation but does not provide kinetic energy storage. Therefore, we will prioritize rotor speed based curtailment over pitch angle based curtailment. In other words, wind power generation is curtailed by increasing the rotor speed beyond the speed corresponding to the maximum power point and pitch angle based curtailment is only used once the rotor speed reaches its maximum speed.

DC power sources: For brevity of the presentation, photovoltaics are used as example for a DC power source. Typically a PV system consists of a two-level DC/AC voltage source converter that modulates the DC voltage v_{dc} into an AC voltage v_{sw}, a PV source, and an optional DC/DC boost converter. Considering the model of a voltage source converter developed above, it remains to model the DC power generation of photovoltaics in response to the DC voltage $v_{\mathsf{pv}} = v_{\mathsf{dc}}$ applied to it. The current $i_{\mathsf{dc}} = i_{\mathsf{pv}}$ and power $P_{\mathsf{pv}} = v_{\mathsf{pv}} i_{\mathsf{pv}}$ are given by the current-voltage characteristic of the PV panel (see Figure 7). For a DC

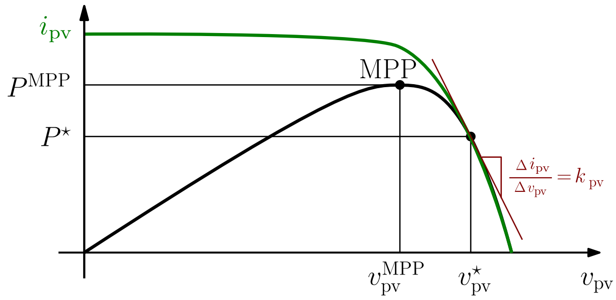

Figure 7: PV operation in the region above the MPP voltage.

voltage setpoint $v^{\star}_{\mathsf{dc}} > v^{\mathsf{MPP}}_{\mathsf{pv}}$ above the MPP voltage $v^{\mathsf{MPP}}_{\mathsf{pv}}$ and fixed solar irradiation, the PV source power characteristics result in proportional control of the DC voltage v_{dc}, i.e., locally around the nominal DC voltage we obtain

$$T_{\mathsf{PV}} \tfrac{\mathrm{d}}{\mathrm{d}t} i_{\mathsf{pv}} = -i_{\mathsf{pv}} + i^{\star} + k_{\mathsf{pv}}(v^{\star}_{\mathsf{dc}})\,(v_{\mathsf{dc}} - v^{\star}_{\mathsf{dc}}), \tag{34}$$

where $i^{\star}$ is the current generated by the PV panel at the voltage $v^{\star}_{\mathsf{dc}}$ and $k_{\mathsf{pv}}(v^{\star}_{\mathsf{dc}}) < 0$ is the sensitivity of the PV current generation with respect to the PV terminal voltage at the nominal operating point $v^{\star}_{\mathsf{dc}}$. Moreover, T_{PV} models the response time of passive filters and/or a DC/DC converter and thus can be used to approximately model both single-stage and dual-stage system. We note that, e.g., fuel cells and battery energy storage systems with DC/DC converter or passive filter can also be modeled by a model of the form (34).

3.1.4 Modeling of complex devices through model composition

The key advantage of the reduced order models presented above is that a wide variety of renewable generation and FACTS devices can be modeled through composition of few reduced order models. For example, a wind turbine with a permanent magnet synchronous machine that is interfaced to the grid through two back-to-back full scale converters can be directly modeled as an interconnection of the mechanical power source model connected to a synchronous machine. In turn, the synchronous machine is connected to the grid through back-to-back DC/AC converters that are interconnected through a DC connection.

Similarly, a voltage source converter HVDC system can be directly modeled by connecting two voltage source converters through a DC connection. In both cases the remaining control inputs in our macroscopic model that contains the internal controls are the AC voltages of the converters. These can be used to implement both grid-forming and grid-following functions. Instead, in this project we will use a unified control that makes power imbalances transparent across the HVDC link so that each side of the HVDC link provides grid support to the other side if needed without a change in the control structure (e.g., switching from grid-following to grid-forming operation).

Another example are static synchronous compensators (STATCOM). STATCOMs are shunt FACTS devices that provide reactive power compensation and voltage support. They consist of a DC/AC converter with a DC capacitor, but no DC power source. For the reactive power regulation the most prominent strategies are grid-following and use PI control to control a DC/AC converter as linear reactive current source to provide voltage support, or controlling a DC/AC converter as non-linear current source to compensate for the non-linear loads, (for details see [39]). In our modeling framework a grid-forming STATCOM can be modeled through the voltage source converter model without DC power source.

3.2 Control and small-signal stability analysis framework

Standard controls for grid-connected voltage source converters typically either assume the AC grid to be stable (grid-following) or the DC voltage to be stable (grid-forming). Instead, we propose a control that stabilizes both the DC and the AC voltage while respecting power balance between the two sides. We will show that this control

1. is agnostic to the location of the converter in the power system as well as the location (i.e., DC terminal or AC terminal) and technology of the power source (i.e., wind turbine, PV, storage),
2. clarifies the impact of power source time constants, power limits, and their inherent energy on system-level stability analysis, and
3. provides the appropriate level of grid-support.

In other words, a PV system provides an inertia response proportional to the capacity of the DC-link capacitor, and provide frequency control if the PV module is operated below the maximum power point (i.e., at a DC voltage above the maximum power point voltage).

We emphasize that these features are achieved without switching the converter controller. This aspect is crucial for resilience, scalability, and analysis. One may be tempted to realize this functionality by switching the converter controls between AC grid-following / DC grid-forming and AC grid-forming / DC grid-following during operation. However, this would require fast, reliable millisecond rate communication throughout a system of potentially millions of distributed renewable sources, result in stability concerns due to the switched dynamics, and in many cases the information required to accurately determine the correct configuration will not be available in real-time. Moreover, analytical and simulation-based stability studies would have to check every possible combination admissible under the switching rules and thereby make stability studies intractable for any system of realistic scale.

3.2.1 Simultaneous AC and DC grid-forming control

As discussed in the introduction a major shortcoming of today's grid-forming and grid-following control is that they assume that either the AC or DC terminal of the converter is stable irrespective of the current drawn/injected by the converter. Figure 8 shows a converter-dominated power system in which DC/AC power converters interface power sources to a power network.

A grid-following converter is shown in Figure 9. It is assumed that, from the viewpoint of the power converter, the power system can be modeled as an AC voltage source with constant voltage magnitude and frequency. The grid-following power converter is controlled to stabilize its DC bus. The power source (e.g., a solar PV system) injects constant power into the DC bus and the power converter will effectively pass on this constant power injection to the system.

In contrast, grid-forming control (see Figure 10) assumes that the power source is controlled to stabilize the DC bus voltage and the power converter modulates the (constant) DC voltage into a stable AC voltage waveform and thereby ensures self-synchronization and supports the power system [8].

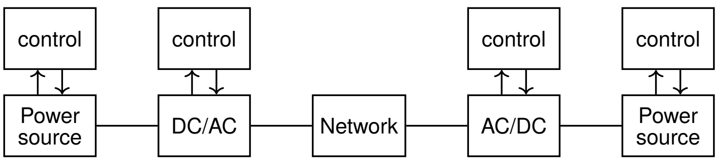

Figure 8: Converter-dominated power system in which DC/AC power converters interface power sources to a power network.

Crucially, both of these control concepts do not account for power balance between the DC and AC terminal, but assume that any power required to balance the DC and AC terminals of the power converter is provided either by the grid (grid-following) or the power source behind the converter (grid-forming). These implicit assumptions result in a control that does not provide grid support even if the power source has this capability and fails if the power system is not stabilized by other devices (grid-following) or a control that provides grid-support but will fail if the power source is not sufficiently controllable (grid-forming) [8]. This lack of controllability could either arise from slow dynamics of the power source, limits on its power generation, or faults in the power source.

Instead, we aim to control the power converter such that power imbalances become transparent between the DC and AC terminal (see Figure 11). In the remainder, we will restrict our attention to two-level voltage source converters. Results for the proposed control paradigms applied to MMCs in the context of HVDC systems can be found in [29]. In this setup, the power converter forms its AC voltage and stabilizes its DC voltage. However, it can only do so if the power between the DC and AC terminal is balanced. To achieve this, the frequency deviation of its AC voltage (i.e., the indicator of power imbalance in AC systems) and the deviation of its DC voltage (i.e., the indicator of power imbalance in a DC system) are tied together through a dynamic controller.

To this end, we propose to use the following controller to determine the AC voltage reference

$$\begin{aligned} \tfrac{\mathrm{d}}{\mathrm{d}t}\theta &= \omega_0 + m_p(P^\star - P_{\text{ac}}) + k_\theta(v_{\text{dc}} - v_{\text{dc}}^\star), && \text{(35a)} \\ \tau_v \tfrac{\mathrm{d}}{\mathrm{d}t}V &= -V + V^\star + m_q(Q^\star - Q), && \text{(35b)} \end{aligned}$$

where m_p denotes the $P_{\text{ac}} - f$ droop gain, m_q denotes the $Q - V$ droop gain, and k_θ is the gain of a DC voltage controller inspired by the controls in [40, 26]. We note that if the DC voltage is tightly controlled by the DC source, then $v_{\text{dc}} \approx v_{\text{dc}}^\star$ and (35) reduces to standard grid-forming droop control [13]. However, if $v_{\text{dc}} \neq v_{\text{dc}}^\star$, the AC voltage frequency $\omega = \frac{\mathrm{d}}{\mathrm{d}t}\theta$ is adjusted to control the DC voltage through the AC terminal. An alternative approach is the energy-balancing controller

$$\begin{aligned} \tfrac{\mathrm{d}}{\mathrm{d}t}\theta &= \omega_0 + m_p \tfrac{\mathrm{d}}{\mathrm{d}t}(v_{\text{dc}} - v_{\text{dc}}^\star) + k_\theta(v_{\text{dc}} - v_{\text{dc}}^\star), && \text{(36a)} \\ \tau_v \tfrac{\mathrm{d}}{\mathrm{d}t}V &= -V + V^\star + m_q(Q^\star - Q). && \text{(36b)} \end{aligned}$$

Note that $\frac{\mathrm{d}}{\mathrm{d}t}v_{\text{dc}} \approx P_{\text{ac}} - P_{\text{ac}}$, i.e., this control aims to balance the DC voltage as well as the power flowing in and out of the converter. The controller (36) can be rewritten without the derivative of the DC voltage

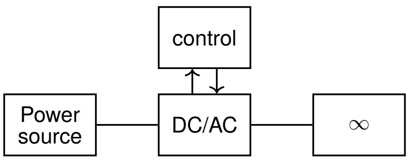

Figure 9: Grid-following power converter control assumes that the power system can be modeled as AC voltage source (i.e., an infinite bus), the power converter stabilizes the voltage of its DC bus, and the power source injects constant power into the DC bus. As a consequence, the grid-following converter will inject constant power into the power network.

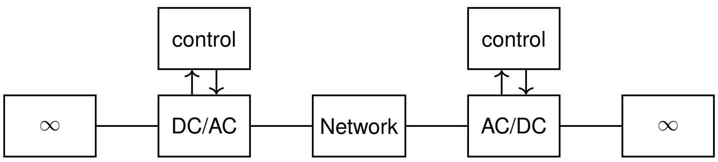

Figure 10: Grid-forming power converter that stabilizes the power system by forming a stable AC voltage waveform. It is assumed that the power source is controlled to stabilize the converter DC bus.

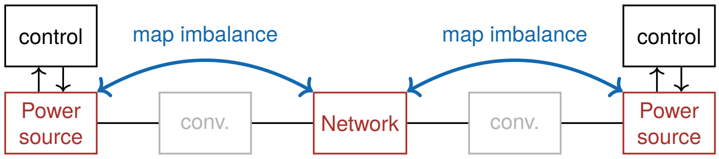

Figure 11: Energy-balancing control maps power imbalances from DC to AC terminal. This enables power sources on both sides of the converter to respond to power imbalances.

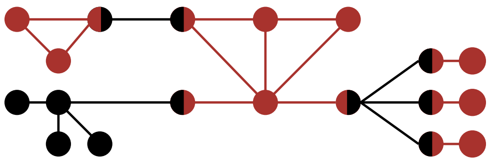

Figure 12: Example of a hybrid AC/DC network topology with AC nodes and lines (red), DC nodes and lines (black), and DC/AC nodes (red/black).

as follows

$$\theta = \theta' + m_p(v_{\text{dc}} - v_{\text{dc}}^\star) \tag{37a}$$
$$\tfrac{\mathrm{d}}{\mathrm{d}t}\theta' = \omega_0 + k_\theta(v_{\text{dc}} - v_{\text{dc}}^\star), \tag{37b}$$
$$\tau_v \tfrac{\mathrm{d}}{\mathrm{d}t} V = -V + V^\star + m_q(Q^\star - Q), \tag{37c}$$

i.e., PI controller of the DC voltage through the AC terminal. While the controls (35) and (36) are superficially similar, they result in significantly different responses. One crucial difference is that, in contrast to (36), the control gains of (35) do not have a clear interpretation and post-event steady-states are hard to determine.

3.2.2 Small-signal modeling framework

In this section, we introduce a tractable reduced-order order model of a power system containing AC and DC transmission, power converters, machines, and renewable and conventional generation. The network is modeled as a connected, undirected, simple graph $\mathcal{G}_N = (\mathcal{N}_N, \mathcal{E}_N)$, where $\mathcal{N}_N := \mathcal{N}_{\text{ac}} \cup \mathcal{N}_{\text{dc}} \cup \mathcal{N}_{\text{c}}$ consists of AC nodes $\mathcal{N}_{\text{ac}}$ corresponding to machines, DC/AC nodes $\mathcal{N}_{\text{c}}$ corresponding to power converters, and DC buses $\mathcal{N}_{\text{dc}}$. We distinguish two types of edges: AC edges $\mathcal{E}_{\text{ac}} \in (\mathcal{N}_{\text{ac}} \cup \mathcal{N}_{\text{c}}) \times (\mathcal{N}_{\text{ac}} \cup \mathcal{N}_{\text{c}})$ corresponding to AC connections, and DC edges $\mathcal{E}_{\text{dc}} \in (\mathcal{N}_{\text{dc}} \cup \mathcal{N}_{\text{c}}) \times (\mathcal{N}_{\text{dc}} \cup \mathcal{N}_{\text{c}})$ corresponding to DC connections. Figure 12 shows an example of a hybrid AC/DC network. Note that the AC and DC edges do not necessarily correspond to transmission lines, but generic AC and DC connections between converters and machines (cf. Figure 14).

Next, we partition the network into an AC network $\mathcal{G}_{\text{ac}} = (\mathcal{N}_{\text{ac}} \cup \mathcal{N}_{\text{c}}, \mathcal{E}_{\text{ac}})$ (red in Figure 12), and a DC network $\mathcal{G}_{\text{dc}} = (\mathcal{N}_{\text{dc}} \cup \mathcal{N}_{\text{c}}, \mathcal{E}_{\text{dc}})$ (black in Figure 12). Even though the overall hybrid network $\mathcal{G}_N$ corresponds to a connected graph, the AC and DC graphs $\mathcal{G}_{\text{ac}}$ and $\mathcal{G}_{\text{dc}}$ are not necessarily connected. Thus, we partition $\mathcal{G}_{\text{ac}}$ into connected components $\mathcal{G}_{\text{ac}} = \bigcup_{i=1}^{N_{\text{ac}}} \mathcal{G}_{\text{ac}}^i$ corresponding to N_{ac} subgrids, i.e., for all $i \in \mathbb{N}_{[1,N_{\text{ac}}]}$, $\mathcal{G}_{\text{ac}}^i = (\mathcal{N}_{\text{ac}}^i \cup \mathcal{N}_{\text{ac/dc}}^i, \mathcal{E}_{\text{ac}}^i)$ where $\mathcal{E}_{\text{ac}}^i$ is the edge set and $\mathcal{N}_{\text{ac}}^i$ and $\mathcal{N}_{\text{ac/dc}}^i$ denote the AC nodes and DC/AC nodes (i.e., the converter nodes from $\mathcal{N}_c$ that are part of the i^{th} AC graph). Analogously, $\mathcal{G}_{\text{dc}} = \bigcup_{i=1}^{N_{\text{dc}}} \mathcal{G}_{\text{dc}}^i$, where for $i \in \mathbb{N}_{[1,N_{\text{dc}}]}$, $\mathcal{G}_{\text{dc}}^i = (\mathcal{N}_{\text{dc}}^i \cup \mathcal{N}_{\text{DC/AC}}^i, \mathcal{E}_{\text{dc}}^i)$. Finally, we note that DC/AC voltage source converters interfacing AC and DC subgrids are part of both their corresponding AC and DC graphs. To account for robustness to topology changes, we require the following assumption.

Assumption 1. ($N-\mu$ connectivity) *Given $\mu_{\mathcal{N}}, \mu_{\mathcal{E}} \in \mathbb{N}_0$, the graph $\mathcal{G}_N$ and its AC components $\mathcal{G}_{\text{ac}}^i$ remain connected when deleting any $\mu_{\mathcal{N}}$ nodes (and their edges) and any $\mu_{\mathcal{E}}$ edges.*

In the remainder of this work, we present conditions on the graph $\mathcal{G}_N$ that will guarantee frequency and DC voltage stability of the power system when deleting $\mu_\mathcal{N}$ nodes and $\mu_\mathcal{E}$ edges.

We use a linear model for the power flow and all variables denote deviations from their linearization point. To every AC node $l \in \mathcal{N}_{\text{ac}}$ we associate a voltage phase angle deviation $\theta_l \in \mathbb{R}$ and a frequency deviation $\omega_l \in \mathbb{R}$; to every DC node $l \in \mathcal{N}_{\text{dc}}$ we associate a DC voltage deviation $v_l \in \mathbb{R}$, and to every DC/AC node $l \in \mathcal{N}_{\text{ac/dc}}$ we associate a voltage phase angle deviation $\theta_l \in \mathbb{R}$ and a DC voltage deviation $v_l \in \mathbb{R}$. To every AC edge $l \in \mathcal{E}_{\text{ac}}$ we assign an active power deviation $P_{\text{ac},l} \in \mathbb{R}$, and to every DC edge $l \in \mathcal{E}_{\text{dc}}$ we assign a power deviation $P_{\text{dc},l} \in \mathbb{R}$. For small phase angle and DC voltage deviations as well as constant AC voltage magnitudes we linearized the power flow model developed in the previous section to obtain

$$P_{\text{ac}} = L_{\text{ac}}\theta + P_{\text{d}_{\text{ac}}}, \tag{38a}$$
$$P_{\text{dc}} = L_{\text{dc}}v + P_{\text{d}_{\text{dc}}}, \tag{38b}$$

where L_{ac} is the Laplacian matrix of the graph $\mathcal{G}_{\text{ac}}$ with AC edge susceptances as edge weights, L_{dc} is the Laplacian matrix of the graph $\mathcal{G}_{\text{dc}}$ with DC edge conductances as edge weights, and the vectors $\theta \in \mathbb{R}^{|\mathcal{N}_{\text{ac}}|+|\mathcal{N}_{\text{c}}|}$ and $v \in \mathbb{R}^{|\mathcal{N}_{\text{dc}}|+|\mathcal{N}_{\text{c}}|}$ collect the AC voltage phase angles and DC voltages of the different nodes. Finally, $P_{\text{d}_{\text{ac}}} \in \mathbb{R}^{|\mathcal{N}_{\text{ac}}|+|\mathcal{N}_{\text{c}}|}$ and $P_{\text{d}_{\text{dc}}} \in \mathbb{R}^{|\mathcal{N}_{\text{dc}}|+|\mathcal{N}_{\text{c}}|}$ model variations in load at the AC and DC nodes.

In the following, we present reduced-order linearized device models that will be used to obtain the overall power system model. Before proceeding, we note that machines and converters have losses that, in theory, render the power system stable. However, in practice, they are often too small (e.g., flywheel friction losses or HVDC converter losses) to rely on them for stability. Therefore, we assume that coefficients D_l and G_l in the following equations that model device losses are only used to model significant damping (e.g., frequency depended loads) and zero for negligible parasitic losses.

Synchronous machines: For all $l \in \mathcal{N}_{\text{ac}}$, we use the second order machine dynamics

$$\tfrac{\mathrm{d}}{\mathrm{d}t}\theta_l = \omega_l, \tag{39a}$$
$$M_l \tfrac{\mathrm{d}}{\mathrm{d}t}\omega_l = -D_l\omega_l + P_l - P_{\text{ac},l}. \tag{39b}$$

Here, $M_l \in \mathbb{R}_{>0}$ and $D_l \in \mathbb{R}_{\geq 0}$ model the machine inertia and losses. Moreover, $P_{\text{ac},l}$ is the AC active power deviation, and $P_l \in \mathbb{R}$ is the deviation of the mechanical power applied to the machine rotor. If the machine is not interfacing generation (e.g., synchronous condenser or flywheel), then $P_l = 0$. Otherwise, we use the turbine model

$$T_{\text{g},l} \tfrac{\mathrm{d}}{\mathrm{d}t} P_l = -P_l - k_{\text{g},l}\omega_l, \tag{40}$$

where $k_{\text{g},l} \in \mathbb{R}_{\geq 0}$ is the linearized sensitivity of the turbine with respect to changes in frequency (e.g., governor gain of a steam turbine) and $T_{\text{g},l} \in \mathbb{R}_{>0}$ is its time constant. As discussed in Sec. 3.1.3, (40) can also be used to model a wind turbine. Figure 13 shows the power generated by a wind turbine with zero blade pitch angle as a function of the rotor speed ω and wind speed [33]. Linearizing at the MPP (circle) results in $k_{\text{g},l} = 0$. Linearizing at a higher turbine speed (triangle) results in $k_{\text{g},l} \in \mathbb{R}_{>0}$, and $T_{\text{g},l} \in \mathbb{R}_{>0}$ is an aerodynamic time constant [41]. A more detailed investigation of the complex dynamics of wind turbines utilizing blade pitch control is seen as an interesting area for future work.

DC nodes and DC sources: For all $l \in \mathcal{N}_{\text{dc}}$, we use the following DC bus dynamics

$$C_l \tfrac{\mathrm{d}}{\mathrm{d}t} v_l = -G_l v_l + P_l - P_{\text{dc},l}, \tag{41}$$

where $C_l = \frac{c_{l,\text{dc}}}{v_l^\star} \in \mathbb{R}_{>0}$, $c_{l,\text{dc}} \in \mathbb{R}_{>0}$ is the DC capacitance, and $v_l^\star \in \mathbb{R}_{>0}$ is the nominal DC voltage. Moreover, $G_l = \frac{g_{l,\text{dc}}}{v_l^\star} \in \mathbb{R}_{\geq 0}$ where $g_{l,\text{dc}} \in \mathbb{R}_{\geq 0}$ is the DC conductance, $P_{\text{dc},l}$ is the deviation of the DC network power injection. If the DC bus is not interfacing generation then $P_l = 0$. Otherwise, we model P_l by

$$T_{\text{g},l} \tfrac{\mathrm{d}}{\mathrm{d}t} P_l = -P_l - k_{\text{g},l} v_l, \tag{42}$$

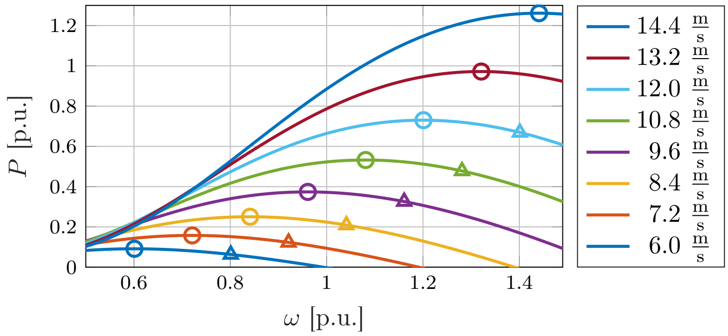

Figure 13: Steady-state power generation P of a wind turbine with zero blade pitch angle as a function of the rotor speed ω and wind speed, MPP (circle), and operating points with power reserves (triangle).

where $T_{\mathsf{g},l} \in \mathbb{R}_{>0}$ is the DC source time constant and $k_{\mathsf{g},l} \in \mathbb{R}_{\geq 0}$ is its sensitivity with respect to the DC voltage. For example, linearizing the power generation of a PV module at the MPP results in $k_{\mathsf{g},l} = 0$, while linearizing at an operating point with power reserves results in $k_{\mathsf{g},l} \in \mathbb{R}_{>0}$ (see Figure 7).

DC/AC voltage source converters: Each DC/AC voltage source converter (VSC) with index $l \in \mathcal{N}_{\mathsf{c}}$ modulates a DC voltage v_l into an AC voltage. The angle and magnitude of the AC voltage are control inputs. For frequency stability analysis of transmission systems, the AC voltage magnitude is typically assumed to be constant [27, Sec. 6]. The dc-link capacitor dynamics are modeled by [26]

$$C_l \tfrac{\mathrm{d}}{\mathrm{d}t} v_l = -G_l v_l + P_l - P_{\mathsf{ac},l} - P_{\mathsf{dc},l}, \tag{43}$$

where $C_l = \frac{c_{l,\mathsf{dc}}}{v_l^\star} \in \mathbb{R}_{>0}$ and $G_l = \frac{g_{l,\mathsf{dc}}}{v_l^\star} \in \mathbb{R}_{\geq 0}$ are the (scaled) DC capacitance and conductance, and P_l, $P_{\mathsf{dc},l}$, $P_{\mathsf{ac},l}$, denote the DC source power and DC and AC network power injections. Note that $P_{\mathsf{ac},l}$ is a function of the angle deviation θ_l. For power converters that do not interface power generation $P_l = 0$, e.g., static synchronous compensators used for reactive power control or HVDC converters [9]. Otherwise, the power generation P_l (e.g., PV modules) is modeled by (42).

Modeling complex systems and devices through model composition: A wide range of complex devices and topologies can be modeled through composition of the models developed in this section. For example, Figure 14 shows a wind turbine interfaced by a synchronous machine and back-to-back power converters. Moreover, an offshore wind farm can be modeled by connecting multiple wind turbines to an AC subgrid that is connected to an onshore AC subgrid through a DC network. The overall power

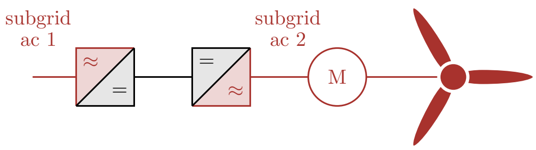

Figure 14: Wind turbine interfaced by a synchronous machine and back-to-back power converters. The connection between the machine and the rotor side converter is modeled through an AC edge and the connection between the power converters is modeled through a DC edge.

system model combines the AC and DC transmission network model (38), synchronous machine model (39), power converter model (43) with the energy-balancing control (35) or (36), and the power source models (40) and (42).

We define a vector $\theta \in \mathbb{R}^{|\mathcal{N}_{\mathsf{ac}} \cup \mathcal{N}_{\mathsf{c}}|}$ that collects the angles of all AC nodes and converter nodes, a vector $\omega \in \mathbb{R}^{|\mathcal{N}_{\mathsf{ac}}|}$ that collects the frequencies of AC nodes, and a vector $v \in \mathbb{R}^{|\mathcal{N}_{\mathsf{c}} \cup \mathcal{N}_{\mathsf{dc}}|}$ that collects the DC voltages of all DC/AC converter nodes and DC nodes. Next, we define the set $\mathcal{N}_{\mathsf{g}} \subseteq \mathcal{N}$ of power sources (i.e., a turbine or a DC power source) that responds to frequency or DC voltage deviations (i.e., $k_{\mathsf{g},i} > 0$ if $i \in \mathcal{N}_{\mathsf{g}}$) and $P \in \mathbb{R}^{|\mathcal{N}_{\mathsf{g}}|}$ collects their power generation. Additionally, the matrix $\mathcal{I}_{\mathsf{g},\mathsf{ac}} \in \{0,1\}^{|\mathcal{N}_{\mathsf{ac}}| \times |\mathcal{N}_{\mathsf{g}}|}$

models the interconnection of machines and stabilizing mechanical power sources and

$$\{\mathcal{I}_{\text{g,ac}}\}_{(i,j)} = \left\{ \begin{array}{ll} 1, & i \in \mathcal{N}_{\text{ac}},\ j \in \mathcal{N}_{\text{g}}, \\ 0, & i \in \mathcal{N}_{\text{ac}},\ j \notin \mathcal{N}_{\text{g}} \end{array} \right\},$$

i.e., a machine with index i is connected to a turbine j with $k_{\text{g},j} > 0$ iff $\{\mathcal{I}_{\text{g,ac}}\}_{(i,j)} = 1$. Similarly, $\mathcal{I}_{\text{g,dc}} \in \mathbb{R}^{|\mathcal{N}_{\text{c}} \cup \mathcal{N}_{\text{dc}}| \times |\mathcal{N}_{\text{g}}|}$ describes which DC/AC and DC nodes are connected to a stabilizing DC power source, i.e.,

$$\{\mathcal{I}_{\text{g,dc}}\}_{(i,j)} = \left\{ \begin{array}{ll} 1, & i \in \mathcal{N}_{\text{c}} \cup \mathcal{N}_{\text{dc}},\ j \in \mathcal{N}_{\text{g}}, \\ 0, & i \in \mathcal{N}_{\text{c}} \cup \mathcal{N}_{\text{dc}},\ j \notin \mathcal{N}_{\text{g}} \end{array} \right\}.$$

Analogously to $\mathcal{I}_{\text{g,ac}}$ and $\mathcal{I}_{\text{g,dc}}$, the matrices $\bar{\mathcal{I}}_{\text{g,ac}} \in \{0,1\}^{|\mathcal{N}_{\text{ac}}| \times |\bar{\mathcal{N}}_{\text{g}}|}$ and $\bar{\mathcal{I}}_{\text{g,dc}} \in \{0,1\}^{|\mathcal{N}_{\text{c}}| \times |\bar{\mathcal{N}}_{\text{g}}|}$ model the interconnection between machines, converters, power sources in $\bar{\mathcal{N}}_{\text{g}}$. For notational convenience, we define matrices $\mathcal{I}_{\text{ac}} \in \{0,1\}^{|\mathcal{N}_{\text{ac}}| \times |\mathcal{N}_{\text{ac}} \cup \mathcal{N}_{\text{c}}|}$ and $\mathcal{I}_{\text{ac/dc}} \in \{0,1\}^{|\mathcal{N}_{\text{c}}| \times |\mathcal{N}_{\text{c}} \cup \mathcal{N}_{\text{ac}}|}$ to extract machine and converter angles from the overall angle vector θ, e.g., $\mathcal{I}_{\text{ac}}\theta$ is the vector of all machine angles. Similarly, $\mathcal{I}_{\text{DC/AC}} \in \{0,1\}^{|\mathcal{N}_{\text{c}}| \times |\mathcal{N}_{\text{c}} \cup \mathcal{N}_{\text{dc}}|}$, and $\mathcal{I}_{\text{dc}} \in \{0,1\}^{|\mathcal{N}_{\text{dc}}| \times |\mathcal{N}_{\text{c}} \cup \mathcal{N}_{\text{dc}}|}$ extract converter DC voltages and DC node voltages from the vector v.

To facilitate the stability analysis in the next section, we change coordinates from absolute angles θ to angle differences i.e., $\eta := B_{\text{ac}}^{\mathsf{T}}\theta$ [42, cf. Sec. III], where $B_{\text{ac}} \in \{-1,0,1\}^{|\mathcal{N}_{\text{ac}} \cup \mathcal{N}_{\text{ac/dc}}| \times |\mathcal{E}_{\text{ac}}|}$ is the incidence matrix of the AC graph $\mathcal{G}_{\text{ac}}$. Finally, the overall model of a hybrid power system and power converters using, e.g., the controller (35) is given by (44) with $T := \operatorname{blkdiag}\{I_{|\mathcal{N}_{\text{ac}} \cup \mathcal{N}_{\text{c}}|}, M, C, T_{\text{g}}, \bar{T}_{\text{g}}\}$ and machine inertia $M := \operatorname{diag}\{M_i\}_{i=1}^{|\mathcal{N}_{\text{ac}}|} \succ 0$, DC capacitance $C = \operatorname{diag}\{C_i\}_{i=1}^{|\mathcal{N}_{\text{c}} \cup \mathcal{N}_{\text{dc}}|} \succ 0$, and power generation time constants $T_{\text{g}} := \operatorname{diag}\{T_{\text{g},i}\} \succ 0$ and $\bar{T}_{\text{g}} := \operatorname{diag}\{T_{\text{g},i}\} \succ 0$. Moreover, $\mathcal{W}_{\text{ac}}$ is a diagonal matrix of AC edge weights, and L_{dc} is the DC graph Laplacian. Finally, $M_p := \operatorname{diag}\{m_{p,i}\}_{i=1}^{|\mathcal{N}_{\text{c}}|} \succ 0$ and $K_\theta := \operatorname{diag}\{k_{\theta,i}\}_{i=1}^{|\mathcal{N}_{\text{c}}|} \succ 0$ collect the converter control gains, $D := \operatorname{diag}\{d_i\}_{i=1}^{|\mathcal{N}_{\text{ac}}|} \succeq 0$ and $G = \operatorname{diag}\{g_i\}_{i=1}^{|\mathcal{N}_{\text{ac/dc}} \cup \mathcal{N}_{\text{dc}}|} \succeq 0$ collect machine and converter losses, and $K_{\text{g}} = \operatorname{diag}\{k_i\}_{i=1}^{|\mathcal{N}_{\text{g}}|} \succ 0$ collects the power source sensitivities.

$$T \frac{\mathrm{d}}{\mathrm{d}t} \begin{bmatrix} \eta \\ \omega \\ v \\ P \end{bmatrix} = \begin{bmatrix} -(\mathcal{I}_{\text{ac/dc}} B_{\text{ac}})^{\mathsf{T}} M_p \mathcal{I}_{\text{ac/dc}} B_{\text{ac}} \mathcal{W}_{\text{ac}} & (\mathcal{I}_{\text{ac}} B_{\text{ac}})^{\mathsf{T}} & (\mathcal{I}_{\text{ac/dc}} B_{\text{ac}})^{\mathsf{T}} K_\theta \mathcal{I}_{\text{DC/AC}} & \mathbb{0}_{(|\mathcal{N}_{\text{ac}} \cup \mathcal{N}_{\text{c}}|) \times |\mathcal{N}_{\text{g}}|} \\ -\mathcal{I}_{\text{ac}} B_{\text{ac}} \mathcal{W}_{\text{ac}} & -D & \mathbb{0}_{|\mathcal{N}_{\text{ac}}| \times |\mathcal{N}_{\text{ac}}|} & \mathcal{I}_{\text{g,ac}} \\ -\mathcal{I}_{\text{DC/AC}}^{\mathsf{T}} \mathcal{I}_{\text{ac/dc}} B_{\text{ac}} \mathcal{W}_{\text{ac}} & \mathbb{0}_{|\mathcal{N}_{\text{c}} \cup \mathcal{N}_{\text{ac}}| \times |\mathcal{N}_{\text{ac}}|} & -G + L_{\text{dc}} & \mathcal{I}_{\text{g,dc}} \\ \mathbb{0}_{|\mathcal{N}_{\text{g}}| \times |\mathcal{N}_{\text{ac}} \cup \mathcal{N}_{\text{c}}|} & -K_{\text{g}} \mathcal{I}_{\text{g,ac}}^{\mathsf{T}} & -K_{\text{g}} \mathcal{I}_{\text{g,dc}}^{\mathsf{T}} & -I_{|\mathcal{N}_{\text{g}}|} \end{bmatrix} \begin{bmatrix} \eta \\ \omega \\ v \\ P \end{bmatrix} \tag{44}$$

3.2.3 Stability conditions

Typically, conditions for frequency stability of multi-converter/multi-machine AC power systems exploit passivity, and do not consider the converter DC side. However, in our setting the DC source and network dynamics play a crucial role and individual devices may not be passive. The framework in [43] does not rely on passivity of the nodes/devices, but aims to establish asymptotic stability and robustness guarantees for multi-converter/multi-machine AC networks with arbitrary connected topologies. While this framework is very general, it is not readily applicable to our setting because we consider multiple disjoint AC and DC networks that are interconnected through power converters. Moreover, the following example demonstrates that, even when restricting the focus to a single multi-machine AC network (i.e., synchronous generators and synchronous condensers), asymptotic stability can, in general, not be guaranteed using only device parameters.

Example 1. (Stability and network parameters) *We consider an AC network that consists of two machines without damping and one machine with damping. The dynamics and network topology are given by*

$$\frac{\mathrm{d}}{\mathrm{d}t} \begin{bmatrix} \eta \\ M\omega \end{bmatrix} = \begin{bmatrix} \mathbb{0}_{2\times 2} & B_{ac}^{\mathsf{T}} \\ -B_{ac}\mathcal{W}_{ac} & -D \end{bmatrix} \begin{bmatrix} \eta \\ \omega \end{bmatrix}, \quad B_{ac} := \begin{bmatrix} 1 & 1 \\ -1 & 0 \\ 0 & -1 \end{bmatrix},$$

with line susceptances $\mathcal{W}_{ac} = \operatorname{diag}\{b_1, b_2\}$ and damping $D = \operatorname{diag}\{d_1, 0, 0\} \succeq 0$. For $b_2/b_1 = m_3/m_2$, the solution of the dynamics starting from the initial condition $\eta(0) = c(\frac{b_2}{b_1}, 0)$ and $\omega(0) = \mathbb{0}_3$ is given by $\zeta = \sqrt{b_1/m_2}$ and $\eta_1(t) = \frac{b_2}{b_1}\cos(\zeta t)$, $\eta_2(t) = -\cos(\zeta t)$, $\omega_1(t) = 0$, $\omega_2(t) = \frac{b_2}{\sqrt{b_1 m_2}}\sin(\zeta t)$, and $\omega_3(t) = -\zeta \sin(\zeta t)$. Thus, the solution does not converge and the system is not asymptotically stable.

In this example, for every choice of machine parameters (i.e., m_1, m_2, m_3, and d_1), there exists network parameters (i.e., b_1 and b_2) such that the multi-machine AC system is not asymptotically stable. In other words, in our setting, stability conditions that only require connectedness of the network can, in general, not be obtained.

To develop stability conditions that account for the full variety of diverse devices on future power systems, we require the following condition that allows to guarantee the stability within each DC network.

Condition 1. (Consistent $v_{\text{dc}} - f$ droop) *For all $i \in \mathbb{N}_{[1,N_{\text{dc}}]}$ and all $(n,l) \in \mathcal{N}^i_{\text{DC/AC}} \times \mathcal{N}^i_{\text{DC/AC}}$ it holds that $k_{\theta,n} = k_{\theta,l} := k^i_\theta$.*

This condition requires the per unit $v_{\text{dc}} - f$ droop gains of devices connected to the same DC subgrid to be equal and ensures a consistent mapping of frequency deviations and DC voltage deviations (i.e., $\omega_l / v_l = k^i_\theta$ for all $l \in N^i_{\text{DC/AC}}$) between AC and DC subgrids at the nominal power flow (i.e., if $P_{\text{ac},l} = 0$). This feature is important to ensure frequency and DC voltage coherency, i.e., that individual converters do not deviate too much from the average frequency (DC voltage) of an AC subgrid (DC subgrid), and avoid excessive power flows due to incoherent frequencies (DC voltages) at different nodes of an AC subgrid (DC subgrid).

Next, in order to guarantee stability, the number of DC power sources or mechanical power sources have to respond to frequency or DC voltage deviation (i.e., have sensitivity $k_{\text{g}} > 0$) or devices inducing significant losses that result in damping needs to be at least $\mu_{\mathcal{N}} + 1$. To formalize this requirement, for all AC subgrids $i \in \mathbb{N}_{[1,N_{\text{ac}}]}$, we define node sets that collect nodes $\mathcal{N}^i_{\text{ac}^{\text{l}}}$ and $\mathcal{N}^i_{\text{ac/dc}^{\text{l}}}$ with significant losses, nodes $\mathcal{N}^i_{\text{ac}^{\text{g}}}$ and $\mathcal{N}^i_{\text{ac/dc}^{\text{g}}}$ that are connected to power sources with $k_{\text{g}} > 0$, and the remaining nodes $\mathcal{N}^i_{\text{ac}^{\text{o}}} = \mathcal{N}^i_{\text{ac}} \setminus (\mathcal{N}^i_{\text{ac}^{\text{l}}} \cup \mathcal{N}_{\text{ac}^{\text{g}}})$, $\mathcal{N}^i_{\text{ac/dc}^{\text{o}}} = \mathcal{N}^i_{\text{ac/dc}} \setminus (\mathcal{N}^i_{\text{ac/dc}^{\text{l}}} \cup \mathcal{N}_{\text{ac/dc}^{\text{g}}})$. Similarly, for each DC subgrid $i \in \mathbb{N}_{[1,N_{\text{dc}}]}$, we define the node sets $\mathcal{N}^i_{\text{dc}^{\text{l}}}$, $\mathcal{N}^i_{\text{DC/AC}^{\text{l}}}$, $\mathcal{N}^i_{\text{dc}^{\text{g}}}$, $\mathcal{N}^i_{\text{DC/AC}^{\text{g}}}$, $\mathcal{N}^i_{\text{dc}^{\text{o}}}$, and $\mathcal{N}^i_{\text{DC/AC}^{\text{o}}}$. The following assumption ensures that at least one device in the entire power system provides frequency or DC voltage damping.

Assumption 2. (Frequency & DC voltage stabilization) *One of the following holds for $\mathcal{G}_N$:*

1. $\exists i \in \mathbb{N}_{[1,N_{\text{ac}}]} : |\mathcal{N}^i_{\text{ac}^g} \cup \mathcal{N}^i_{\text{ac}^l} \cup \mathcal{N}^i_{\text{ac/dc}^l} \cup \mathcal{N}^i_{\text{ac/dc}^g}| > \mu_{\mathcal{N}}$,
2. $\exists i \in \mathbb{N}_{[1,N_{\text{dc}}]} : |\mathcal{N}^i_{\text{DC/AC}^g} \cup \mathcal{N}^i_{\text{DC/AC}^l} \cup \mathcal{N}^i_{\text{dc}^l} \cup \mathcal{N}^i_{\text{dc}^g}| > \mu_{\mathcal{N}}$.

As illustrated in Example 1, in general one cannot expect to find conditions that ensure stability for all connected network topologies. To formalize the stability conditions on the network topology and clarify the roles of different devices, the nodes in each AC subgrid are partitioned into different groups depending on whether an AC subgrid has fewer converters than machines (i.e., machine-dominated) or more converters than machines (i.e., converter-dominated).

Definition 1. (Partitioning of $\mathcal{N}^i_{\text{ac}}$) *For every AC subgrid $i \in \mathbb{N}_{[1,N_{\text{ac}}]}$ of $\mathcal{G}_N$ we partition $\mathcal{N}^i_{ac} \cup \mathcal{N}^i_{ac/dc}$ as follows:*

1. $|\mathcal{N}^i_{\text{ac/dc}}| + \mu_{\mathcal{N}} < |\mathcal{N}^i_{\text{ac}}|$: $\mathcal{D}^i := \mathcal{N}^i_{ac^l} \cup \mathcal{N}^i_{ac^g} \cup \mathcal{N}^i_{ac/dc^l} \cup \mathcal{N}^i_{ac/dc^g}$, $\mathcal{C}^i := \mathcal{N}^i_{ac^o}$, *and* $\mathcal{F}^i = \mathcal{N}^i_{ac/dc^o}$,
2. $|\mathcal{N}^i_{\text{ac/dc}}| \geq |\mathcal{N}^i_{\text{ac}}| + \mu_{\mathcal{N}}$: $\mathcal{D}^i := \mathcal{N}^i_{ac/dc}$, $\mathcal{C}^i := \mathcal{N}^i_{ac}$, *and* $\mathcal{F}^i = \emptyset$.

Broadly speaking, we leverage the properties of the nodes $\mathcal{D}^i$ to establish synchronization of the nodes $\mathcal{C}^i$ and stability the overall system. To this end, we first define the subgraph $\bar{\mathcal{G}}^i_0$.

Definition 2. (Reduced AC subgrid graph) *For all $i \in \mathbb{N}_{[1,N_{\text{ac}}]}$, we define the graph $\bar{\mathcal{G}}^i_0$ with node set $\bar{\mathcal{N}}_0 := \mathcal{N}^i_{ac} \cup \mathcal{N}^i_{ac/dc}$ and edge set $\bar{\mathcal{E}}_0 := \mathcal{E}^i_{ac} \setminus ((\mathcal{C}^i \times \mathcal{C}^i) \cup (\mathcal{D}^i \times \mathcal{D}^i))$.*

Notably, for a converter-dominated subgrid, the graph $\bar{\mathcal{G}}_0^i$ only contains connections between converters and machines. On the other hand, for a machine-dominated subgrid, the graph $\bar{\mathcal{G}}_0^i$ only contains connections between devices that contribute to stabilizing frequency and devices that do not.

Finally, Algorithm 1 identifies AC subgrid topologies for which stability can be guaranteed independently of the exact parameters of the connections (i.e., edge weights). To this end, a node $l \in \mathcal{N}$ is defined to be a single-edge node iff there exists only one $j \in \mathcal{N}$ s.t. $(l,j) \in \mathcal{E}$. Moreover, we define $\mu_{\max} := \max\{\mu_{\mathcal{N}}, \mu_{\mathcal{E}}\}$. Algorithm 1 iteratively removes nodes from $\bar{\mathcal{G}}_0^i$ in $\mathcal{C}^i$ for which frequency synchronization to a node in $\mathcal{D}^i$ can be guaranteed, e.g., in a converter-dominated subgrid, machines that synchronize with AC/DC converters are deleted. In a machine-dominated subgrid, machines that do not stabilize frequency but synchronize to converters or machines that stabilize frequency are deleted. Broadly speaking, the algorithm terminates with $\bar{\mathcal{C}}_K^i = \emptyset$, if devices that do not contribute to stabilizing frequency are sufficiently well connected to devices that stabilize frequency.

Algorithm 1 Node removal for $i \in \mathbb{N}_{[1,N_{\text{ac}}]}$

1: **Set** $\bar{\mathcal{G}}_0^i$ as in Definition 2, $\bar{\mathcal{C}}_0^i := \mathcal{C}^i$, and $k := 0$
2: **while** there exists $\mu_{\max} + 1$ single-edge nodes $l \in \mathcal{D}^i$ with an edge to a node $j \in \bar{\mathcal{C}}_k^i$ **do**
3: $\quad \bar{\mathcal{C}}_{k+1}^i := \bar{\mathcal{C}}_k^i \setminus \{j\}$
4: $\quad \bar{\mathcal{E}}_{k+1} := \bar{\mathcal{E}}_k \setminus \{(l,j)\}$, where $(l,j) \in \bar{\mathcal{E}}_k \cap (\mathcal{D}^i \times \bar{\mathcal{C}}_k^i)$
5: $\quad \bar{\mathcal{N}}_{k+1}^i := \bar{\mathcal{N}}_k^i \setminus \{j\}$, $\bar{\mathcal{G}}_{k+1}^i = (\bar{\mathcal{N}}_{k+1}^i, \bar{\mathcal{E}}_{k+1}^i)$
6: $\quad k := k+1$
7: **end while**

Applying Algorithm 1 to simple network structures (e.g., cycle graphs) and stability of the system with nominal graph ($\mu_{\max} = 0$) results in the following corollary that highlights the importance of edges between nodes in $\mathcal{C}^i$ and $\mathcal{D}^i$.

Corollary 1. (Simple network structures) *For $\mu_{\max} = 0$ and all $i \in \mathbb{N}_{[1,N_{\text{ac}}]}$, if every node in $\mathcal{C}^i$ either*

1. *has an edge to a single-edge node in $\mathcal{D}^i$, or*
2. *is part of a cycle that contains a node from $\mathcal{C}^i$ that has an edge to a single edge-node in $\mathcal{D}^i$,*

then there exists $K^i \in \mathbb{N}$ such that Algorithm 1 terminates with $\bar{\mathcal{C}}_{K^i}^i = \emptyset$.

In the most general case (e.g., allowing for synchronous condensers), the stability conditions depend on the system topology. By posing stronger requirements on the devices contained in each AC subgrid, the following topology independent result can be obtained.

Corollary 2. (Topology indepdent conditions) *If Condition 1 and Assumption 1 and 2 hold, and for all $i \in \mathbb{N}_{[1,N_{\text{ac}}]}$ either $\mathcal{N}_{\text{ac}}^i = \emptyset$ or $\mathcal{N}_{\text{ac}^\circ}^i = \emptyset$ holds, then, all systems obtained by deleting at most $\mu_{\mathcal{N}}$ nodes and $\mu_{\mathcal{E}}$ edges from* (44) *are asymptotically stable with respect to the origin.*

The conditions of Corollary 2 impy that $\mathcal{C}^i = \emptyset$ for all $i \in \mathbb{N}_{[1,N_{\text{ac}}]}$ and the proof immediately follows from the fact that Algorithm 1 terminates at the first iteration. Specifically, Corollary 2 requires that each AC network $i \in \mathbb{N}_{[1,N_{\text{ac}}]}$ either (i) only contains converters (i.e., $\mathcal{N}_{\text{ac}}^i = \emptyset$), or (ii) all machines are equipped with a turbine governor system or have significant losses (i.e., $\mathcal{N}_{\text{ac}^\circ}^i = \emptyset$).

We emphasize that Corollary 2 with $\mathcal{N}_{\text{ac}}^i = \emptyset$ $i \in \mathbb{N}_{[1,N_{\text{ac}}]}$ and no DC networks recovers standard conditions for stability of networks of ac-GFM converters with the DC terminal modeled as constant voltage source. However, in addition, Corollary 2 also includes machines, converters interfacing renewable generation with limited flexibility, and DC transmission. Moreover, the dual-port GFM control allows to establish topology indepdent stability conditions for hybrid AC/DC power systems. In contrast, using standard ac-GFM (droop) and ac-GFL (PLL-based) controls requires assigning ac-GFM and ac-GFL controls to each converter interfacing AC and DC networks, which typically requires knowledge of the system topology [9].

We can now state the following stability result for the controller (35).

Theorem 1. (Stability of hybrid AC/DC power systems) *Assume that all power converters use the controller* (35). *If for all $i \in \mathbb{N}_{[1,N_{\text{ac}}]}$, there exists $K^i \in \mathbb{N}$ such that Algorithm 1 terminates with $\bar{\mathcal{C}}^i_{K^i} = \emptyset$ and Condition 1 and Assumptions 1 and 2 hold, then all systems obtained by deleting at most $\mu_{\mathcal{N}}$ nodes and $\mu_{\mathcal{E}}$ edges from* (44) *are asymptotically stable with respect to the origin.*

Detailed proofs can be found in [44]. Theorem 1 guarantees synchronization within each AC subgrid and Condition 1 guarantees synchronization within each DC subgrid. Moreover, Assumption 2 is used to establish that at least one frequency deviation or DC voltage deviation converges to zero. Together with frequency and DC voltage synchronization, this establishes stability of the overall hybrid AC/DC power system (44). Notably, our conditions do not restrict the network parameters of AC subgrids that only contain converters (i.e., $\mathcal{N}^i_{\text{ac}} = \emptyset$). Broadly speaking, the angle differences within such an AC subgrid are fully controlled through the power-balancing dual-port GFM controller and synchronize independently of the network parameters.

The stability conditions for the controller (36) provide further insights into the relationship of the control gains and physical parameters. In particular, we require that the control gain $m_{p,l}$ is proportional to the capacitance of the DC-link capacitor, i.e., $m_{p,l} = \rho C_l$, where $\rho \in \mathbb{R}_{>0}$ is a design parameter. Moreover, we assume that the steady-state $P_{\text{ac}} - f$ droop coefficient $f_{\text{dr}} = k_{\theta,l}/k_{\text{g},l}$ of power converters connected to a DC power source with non-zero sensitivity k_{g} is constant.

Theorem 2. (Stability of hybrid AC/DC power systems) *Assume that all power converters use the controller* (36). *If, in addition to the conditions of Theorem 1, it holds for all $l \in \mathcal{N}^g_{\text{ac/dc}}$ that $4 f_{\text{dr}} < \rho$ and, on every DC subnetwork $i \in \mathbb{N}_{[1,N_{\text{dc}}]}$ it holds that $k^i_\theta < \frac{1}{4 - f_{\text{dr}}\rho} \sigma_{\max}(L^i_{\text{dc}})$, then the overall power system asymptotically stable with respect to the origin.*

Here, $\sigma_{\max}(L_{\text{dc}})$ is the largest singular value of the DC network Laplacian and increases with increasing connectivity. In other words, increased DC network connectivity allows for larger control gains $k_{\theta,l}$. Moreover, a larger gain $m_{p,l}$ relative to the capacitance C_l of the DC-link capacitor, allows for a larger steady-state droop coefficient f_{dr}.

3.2.4 Illustrative examples for the topological stability conditon

To illustrate the topological stability conditons, we consider the converter-dominated and machine-dominates subgrids shown in Figure 15 and the back-to-back wind turbine shown in Figure 14. In all of these cases the seemingly complicated topological stability conditions can be easily verified.

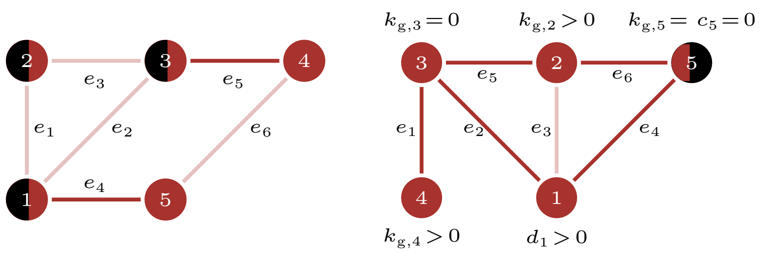

(a) (b)

Figure 15: Examples for a converter-dominated AC subgrid (a) and machine-dominated AC subgrid (b). Edges not contained in $\bar{\mathcal{G}}^i_0$ are shown in light red.

Converter-dominated AC subgrid: applying Definition 1.2 and Definition 2, $\mathcal{C} = \{4, 5\}$, $\mathcal{D} = \{1, 2, 3\}$, and $\bar{\mathcal{E}}_0 = \{e_4, e_5\}$ holds. Hence, in $\bar{\mathcal{G}}^i_0$, the nodes $\{1, 3\} \in \mathcal{C}$ are single-edge nodes and from Corollary 1.1 it directly follows that there exists $K^i \in \mathbb{N}$, such that Algorithm 1 terminates with $\bar{\mathcal{C}}^i_{K^i} = \emptyset$.

Machine-dominated AC subgrid: applying Definition 1.1 we obtain $\mathcal{C} = \{3\}$, $\mathcal{D} = \{1, 2, 4\}$, $\mathcal{F} = \{5\}$, where, e.g., node 3 models a synchronous condenser and node 5 models a STATCOM, HVDC converter, or PV operating at its MPP. Using Definition 2 it follows that $\bar{\mathcal{E}}_0 = \{e_1, e_2, e_4, e_5, e_6\}$ and $\bar{\mathcal{G}}_0$ contains a cycle in which a node from $\mathcal{C}$ has an edge to a single-edge node from $\mathcal{D}$. From Corollary 1.2, there exists $K^i \in \mathbb{N}$, such that Algorithm 1 terminates with $\bar{\mathcal{C}}^i_{K^i} = \emptyset$.

Wind turbine or flywheel energy storage with back to back converter: Irrespective of the operating point of the wind turbine (i.e., $k_{\text{g}} = 0$ or $k_{\text{g}} > 0$), the subgrid ac 2 in Figure 14 is converter-dominated and Corollary 1.2 trivially applies. This result also applies to common flywheel energy storage systems (i.e., Figure 14 without the wind turbine). In addition, for AC 1 we require existence of $K^1 \in \mathbb{N}$ such that Algorithm 1 terminates with $\bar{\mathcal{C}}^1_{K^1} = \emptyset$, and that the converter DC voltage - frequency droop gains satisfy Condition 1.

Offshore wind farm: in an offshore wind farm containing wind turbines with back to back converters, the subgrid ac 1 in Figure 14 only contains the grid-side converters of the wind turbines and an HVDC converter. In other words, $\mathcal{N}^1_{\text{ac}} = \emptyset$, and we only require condition 1 for the DC networks and for ac 1 we require existence of $K^1 \in \mathbb{N}$ such that Algorithm 1 terminates with $\bar{\mathcal{C}}^1_{K^1} = \emptyset$.

3.2.5 Case studies

A case study that combines AC and DC transmission as well as conventional generation and PV is used to illustrate the performance and stability conditions for the controller (35). To this end, consider the power system shown in Figure 16 that consists of two IEEE-9 bus systems (AC 1 and ac 2) interconnected by an HVDC link (DC 1). The first AC subgrid contains conventional thermal generation (TG) interfaced by a synchronous machine (SM) with automatic voltage regulator (AVR) and power system stabilizer (PSS), a two-level voltage source converter (VSC) that interfaces a controllable DC source (e.g., a large-scale battery), a VSC that interfaces photovoltaics (PV), and a VSC that interfaces the subgrids ac 1 and dc 1. The HVDC link has a length of 310 km and connects the subgrid ac 1 that has significant frequency control reserves (i.e., thermal generation and controllable DC source) with the subgrid ac 2 that only contains renewable generation (i.e., PV) interfaced by VSCs and a synchronous condenser (SC). A detailed description of the system parameters and control gains can be found in [44]. Notably, PV$_2$ and PV$_3$ operate above the MPP voltage to provide primary control (i.e., $k_{\text{g}} > 0$) while PV$_1$ operates at the MPP (i.e., $k_{\text{g}} = 0$). Finally, it is straightforward to verify that the topological stability conditions are satisfied (see [44] for further details). We emphasize that a mix of at least four different conventional GFM and GFL controls would be needed to operate this system. Finally, we use an EMT simulation to illustrate and validate the results. AC lines and the DC cables are modeled using the standard π-line dynamics [27, 45] and transformers are explicitly modeled using dynamical models. The simulation uses an 8^{th} order synchronous machine model with AC1A exciter model and automatic voltage regulator. In addition, the machine in ac 1 features a delta-omega power system stabilizer, and first order turbine model with 5% speed droop and the converter control gains are shown in Figure 16.

Starting from steady-state at $t = 0$ s, we simulate a load-step of 0.5 p.u. at bus 17 and $t = 5$ s, next, at $t = 30$ s the power set-points of the turbine, DC source, and converters, are updated to return the system to the nominal frequency. The resulting deviations of the frequency, DC voltage, active power, AC voltage, and the reactive power from their set-points is shown in Figure 17. We emphasize that the 0.5 p.u. load step is very large and pushes the system to the boundary of the normal operating range. Nonetheless, the system dynamics are well-behaved. As predicted, power imbalances propagate to all AC and DC sugrids and the power sources share the additional load after the load step according to their sensitivities and converter control gains. The synchronous machine in ac 1 and VSC$_4$ provide primary frequency control (i.e., VSC$_4$ exihibits ac-GFM functions). Moreover, the PV systems PV$_2$ and PV$_3$ in the subgrid ac 2 increase their power generation and operate closer to their limit (MPP). In other words, we observe that the converter interfacing power generation with available headroom provide grid-support analogous to standard ac-GFM control. In contrast, the power generation of PV$_1$ is approximately constant and resembles an ac-GFL control with maximum power point tracking. In other words, the dual-port GFM control keeps the power output of PV$_1$ approximately at the MPP. Finally, by mapping power imbalances between ac 1 and ac 2 the VSC-HVDC system autonomously leverages the reserves in ac 1 to provide GFM functions to ac 2. While standard VSC-HVDC controls require assigning GFM and GFL functions of the VSCs at the design stage [9], the proposed dual-port GFM control law inherently achieves the

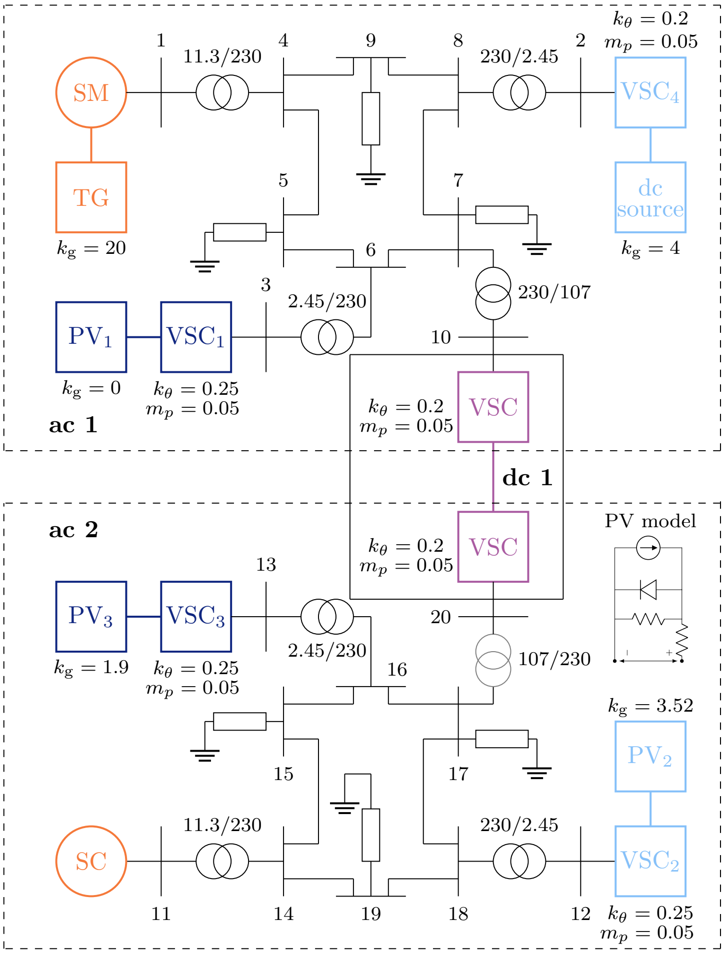

Figure 16: Power system with AC transmission, DC transmission, power converters, machines, photovoltaics, and conventional generation. The control gains and power source sensitivities are shown in per unit, and the base voltages for each transformer side are shown in Kilovolt.

desired behavior without assigning GFM and GFL roles by mapping power imbalances between the areas. After the set-point update additional generation is provided by the turbine governor system and DC source in ac 1 while the PV system returns to its nominal operating point. One key drawback of the controller (35) is that the frequencies in the area ac 1 and ac 2 after the load step are not synchronous. In fact, the explicit $P_{\text{ac}} - f$ droop term in (35) complicates the post-event steady-state response and induces a frequency offset depending on the deviation from the schedule power flow (see [44, 29] for a detailed discussion). In contrast, the controller (36) ensures synchronization in steady-state across DC networks that are connected through DC networks. Corresponding simulation results are shown in Figure 18. The results in Figure 17 also show that despite a 5% droop coefficient on all converters, the effective steady-state droop of (35) is not 5% but modified by the DC voltage control term. In contrast, the controller (36) can be directly tuned to achieve the desired steady-state droop (5% in our case) by selecting k_θ for each converter such that k_θ/k_{g} equals the desired steady-state droop.

Finally, to illustrate that the proposed controller can be applied to a wide range of devices, we replace the synchronous condenser in area ac 2 with a permanent magnet synchronous machine wind turbine with back-to-back converters and again use the controller (36). Simulation results for a load step at bus 17 are shown in Figure 19. It can be seen that the wind turbine provides a significant inertia response achieved by decelerating the rotor to a new operating point with increased power generation.

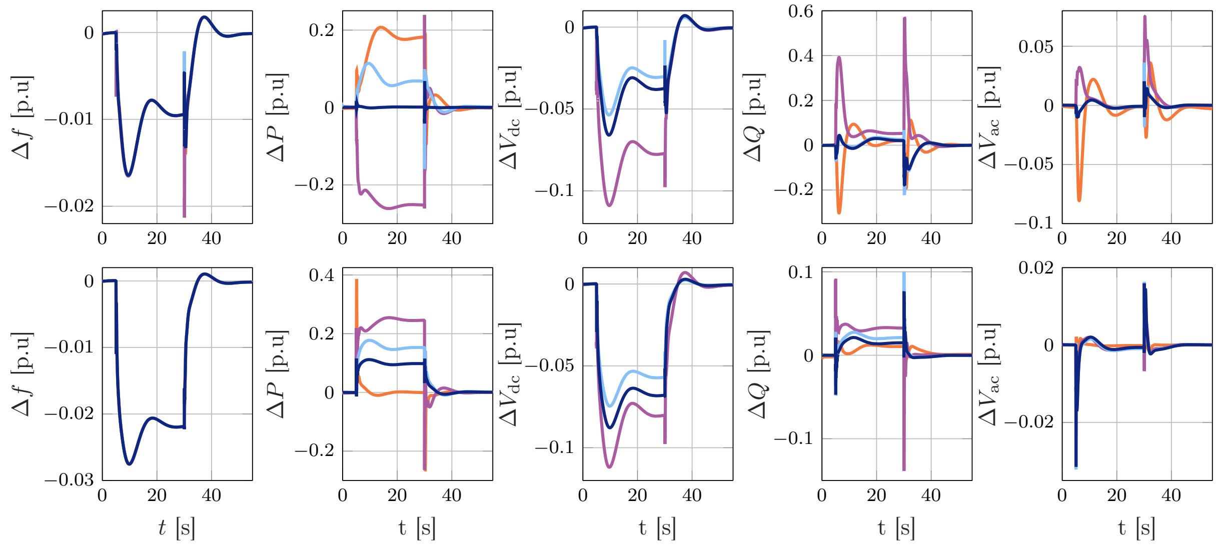

Figure 17: Simulation results for a 0.5 pu load step at bus 17 and subsequent redispatch of the power system in Figure 16 using the controller (35). The plots show the deviation from the setpoints for each device in ac 1 (top) and ac 2 (bottom). The color-scheme is identical to Figure 16.

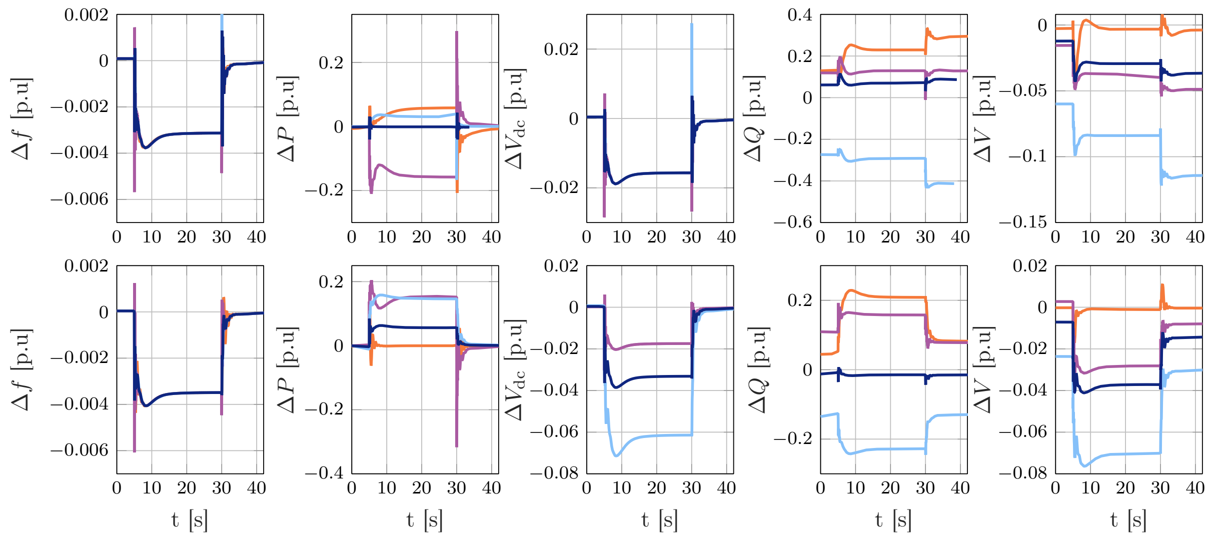

Figure 18: Simulation results for a 0.5 pu load step at bus 17 and subsequent redispatch of the power system in Figure 16 using the controller (36). The plots show the deviation from the setpoints for each device in ac 1 (top) and ac 2 (bottom). The color-scheme is identical to Figure 16.

3.2.6 Discussion and comparison

Comparing the practical and theoretical properties of the controls (35) and (36) in a variety of application scenarios we conclude that the energy-balancing control (36) has significant advantages over the droop-like controller (35). From a theoretical point of view, the droop-like controller (35) appears to have less restrictive stability conditions. However, stability of the overall system does not imply that the system or devices meet common performance specifications. In particular, a system operator may prescribe steady-state droop specifications, inertia specifications, and requires simple aggregate models of the system response for planning. All of these aspects are complicated by the dependence of the frequency of (35) on the difference of the converter power injection from its setpoint. For instance, the steady-state

$P_{\text{ac}} - f$ droop gain (i.e., when $\frac{\mathrm{d}}{\mathrm{d}t} v_{\text{dc}} = 0$) of a converter with DC power source with $k_{\text{g}} > 0$ using the droop-like controller (35) is given by [44]

$$\omega_l = -\left(m_{p,l} + \frac{k_{\theta,l}}{k_{\text{g},l}} \right) P_{\text{ac},l}. \tag{45}$$

Notably, the control gains $m_{p,l}$ and $k_{\theta,l}$ both impact the steady-state response as well as the dynamic performance and it can be difficult to chose the parameters to satisfy both steady-state specifications and achieve good dynamic performance (see e.g. [29]). For example, for typical values the steady-state droop specification $f_{\text{dr}} = m_{p,l} + \frac{k_{\theta,l}}{k_{\text{g},l}}$ for a given droop coefficient f_{dr} can result in values $m_{p,l}$ and $k_{\theta,l}$ that are too small and result in degraded dynamic performance (e.g., oscillations during transients). In contrast, for the energy-balancing control (36) the control gains have well-defined roles and the gain $m_{p,l}$ can be selected based on the DC-link capacitor size to achieve good dynamic performance, while $k_{\theta,l}$ can be directly selected based on steady-state specifications. Specifically, the the steady-state $P_{\text{ac}} - f$ droop gain (i.e., when $\frac{\mathrm{d}}{\mathrm{d}t} v_{\text{dc}} = 0$) of a converter with DC power source with $k_{\text{g}} > 0$ using the droop-like controller (36) is given by

$$\omega_l = -\frac{k_{\theta,l}}{k_{\text{g},l}} P_{\text{ac},l} \tag{46}$$

and, given $k_{\text{g},l}$, one can directly select $k_{\theta,l}$ to achieve a desired steady-state droop gain f_{dr}. Moreover, given $k_{\theta,l}$, the amount of short-term energy storage (i.e., the capacitance C_l of the DC-link capacitor) and droop gain f_{dr} immediately result in a range for $m_{p,l}$ (cf. Theorem 2). Similar results can be obtained for the aggregate system-level response, i.e., for the droop-like controller (35) the steady-state frequency in response to power imbalances generally has an intricate dependence on $m_{p,l}$, $k_{\theta,l}$, and the power exchange through DC networks [44]. In contrast, using the energy-balancing controller (36), all frequency / DC voltage deviations synchronize and all power sources respond. In other words, the steady-state frequency response to power imbalances is simply equal to the sum of all steady-state devices responses irrespective if they are located in an AC or DC network.

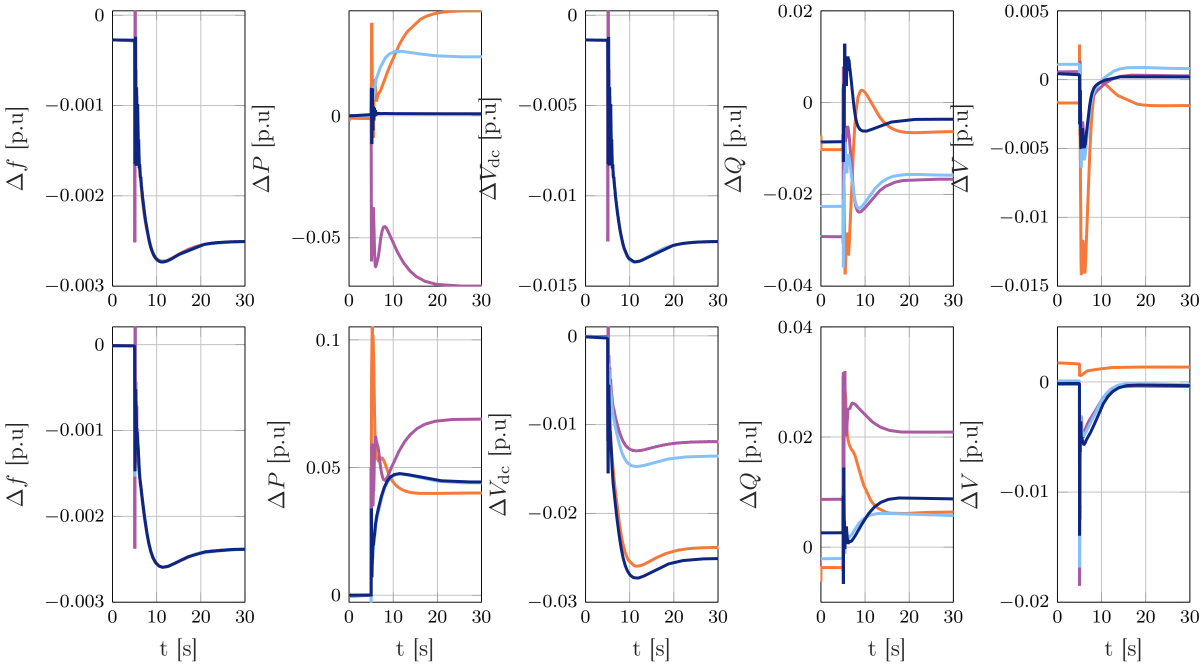

Figure 19: Simulation results for a $0.2\ \text{pu}$ load step at bus 17 of the power system in Figure 16 with wind turbine instead of the synchronous condenser and using the controller (36). The plots show the deviation from the nominal operating point for each device in ac 1 (top) and ac 2 (bottom). The color-scheme is identical to Figure 16.

Finally, from an operational point of view a key advantage of the energy-balancing controller (36) is that only requires a DC voltage setpoint for each converter but not an active power setpoint and thereby clearly accounts for the role of different devices. This highlights that power electronic converters do not generate active power but merely convert it. Instead, the active power generation by power generation devices need to be dispatched. Therefore, power converters and renewable generation using energy-balancing control (36) is more amenable to integration into existing secondary and tertiary control schemes. Therefore, the remainder of this report will focus on the energy-balancing controller (36).

3.3 Secondary control

Today, secondary frequency control relies on a slow centralized proportional-integral (PI) controller for each area of a large-scale power system. The centralized PI controller measures frequency and re-dispatches conventional power generation (e.g., hydro or steam turbines) interfaced by synchronous machines to return the system to its nominal frequency. Conceptually, every machine governor could be replaced by a PI controller, however it is well documented that any offset in local frequency measurements will result in instability [46]. In contrast, for power converters using the controller developed in this project the frequency is a software variable and not subject to measurement offsets. Moreover, in contrast to a machine, grid-forming controls studied in this report explicitly (e.g., (35)) and implicitly (e.g., (36)) feedback power differences to the angle dynamics to achieve angle synchronization. Because of this, small drifts in the microprocessor clocks used to compute the AC voltage waveform will not result in an outright a loss of synchronization.

Conceptually, the purpose of secondary frequency control is to return the system to its nominal frequency and, implicitly, rebalance the short-term energy storage (i.e., kinetic energy of the machine rotors) in the system. In the context of energy-balancing control (36) one could instead aim to rebalance the short-term energy storage elements (i.e., DC-link capacitors and wind turbine rotor speeds) and thereby implicitly return the system frequency to its nominal value. For example, for a photovoltaic system one could use a slow acting proportional-integral controller that updates the set-point $v_{\mathsf{dc}}^\star$ until the error $v_{\mathsf{dc}} - v_{\mathsf{dc}}^\star$ is zero and this implicitly results in the converter modulating a voltage with the nominal frequency. Notably, DC voltage measurement offsets do not impact this approach because the same DC voltage measurement is used in the decentralized secondary controller and the grid-forming control, i.e., it would result in steady-state offsets of the DC voltage but not the AC frequency.

However, from an operational perspective, a key feature of today's secondary control is that it only responds to contingencies within its own area (so called non-interacting control). Because measurements of inter area flows are needed to achieve this functionality, it cannot be provided by a fully decentralized secondary control mechanism. Ultimately, the tie-line-bias control provided by today's secondary control cannot be realized without broadcasting the difference of tie-line flows to their schedule values to every decentralized secondary controller. One potential solution is to split the secondary control action into a fast acting decentralized and slow acting centralized part. The communication requirements of such a scheme would be at least as high as those of today's secondary control that broadcasts signals to all secondary control units without offering any significant advantages over prevailing operator practices. Therefore, we will instead focus on how power converters and renewable generation using energy-balancing control (36) can be integrated into standard secondary control mechanisms.

Standard secondary control relies on the area control error (ACE) defined by for each area by

$$y_{\mathsf{ACE},i} = P_{T,i} - P_{T,i}^\star + B_i(\omega - \omega_0), \tag{47}$$

where $P_{T,i}$ is the power exchange with other areas and $P_{T,i}^\star$ is the schedule power exchange with other areas. Moreover, B_i is the balancing authority bias and typically selected to be equal to the aggregate primary frequency control gain of each area to ensures that secondary control only responds to contingencies in its own area Typically, a proportional-integral controller

$$P_{s,i} = \beta_i y_{\mathsf{ACE},i} x_I, \qquad T_{s,i} \tfrac{\mathrm{d}}{\mathrm{d}t} x_I = y_{\mathsf{ACE},i} \tag{48}$$

is used to compute the incremental change $P_{s,i}$ in power generation in the area. This, change in power generation is then distributed to each unit participating in secondary control based on participation factors α_l, i.e., the update to the power setpoint of the device with index l would be $-\alpha_l P_{s,i}$. Next, we note that energy-balancing control does not require a power setpoint and instead, relies on dispatching the renewable generation through an appropriate choice of DC voltage setpoint (e.g., photovoltaics) or rotor speed and pitch angle (e.g., wind turbines). Specifically, updated DC-voltage and rotor speed setpoints can be directly computed by each unit based on the sensitivities k_{g} of the renewable power generation introduced in the previous sections. For example, for a single-stage PV systems, the incremental change of the DC voltage setpoint is given by $\Delta v^{\star}_{\text{dc},l} = \frac{\alpha_l}{k_{\text{g},l}} P_{s,i}$. In other words, the proposed grid-forming control is directly compatible with prevailing secondary control mechanisms.

Typically, sufficient secondary control reserves are acquired through market mechanisms to ensure that each control area can be re-balanced for credible contingencies. However, when renewable generation participates in secondary control their uncertainty may result in insufficient control reserves. This could be addressed requiring renewable generation to only bid control reserves they can guarantee based on forecasts and historical data. However, this approach may result in very conservative bids [47]. Another approach is to use anti-windup feedback to the secondary controller to ensure stable operation at a non-nominal frequency if all secondary control units have exhausted their flexibility. This results in

$$P_{s,i} = \beta_i y_{\text{ACE},i} + x_I, \qquad T_{s,i} \tfrac{\mathrm{d}}{\mathrm{d}t} x_I = y_{\text{ACE},i} - k_{\text{aw}} \left(P_{s,i} - \operatorname{sat}^{P_{\max,i}}_{P_{\min,i}} (P_{s,i}) \right) \tag{49}$$

In principle, the bound $P_{\max,i}$ on the aggregate secondary control reserves could be determined through real-time communication of the available headroom of each secondary control unit. However, this approach does not scale well with the number of devices. Instead, we assume that each secondary control unit bids a percentage of its predicted maximum power point as control reserves. The system operator can then use prediction models to provide a lower bound for the aggregate secondary control reserves to be used in the secondary controller. The key advantage of this approach is that uncertainty does not have to be quantified for each device, but only for the entire fleet of secondary control units. In future systems a large number of heterogeneous devices are envisioned to contribute to secondary control and thereby reduce the uncertainty of the aggregate secondary control reserves through geographical and technological diversity. Crucially, this approach does not require bi-directional communication with secondary control units but only requires broadcasting the signal $P_{s,i}$. To illustrate the secondary control response resulting from (49) and using $\Delta v^{\star}_{\text{dc},l} = \frac{\alpha_l}{k_{\text{g},l}} P_{s,i}$ to update the DC voltage setpoint of a single-stage PV system, we divide the system ac 1 in Figure 16 into two areas at bus 4 and disconnect the HVDC link. In other words, one area contains the synchronous machine, while the second area contains two power converters. Simulation results for a load step at bus 7 are shown in Figure 20 and Figure 21.

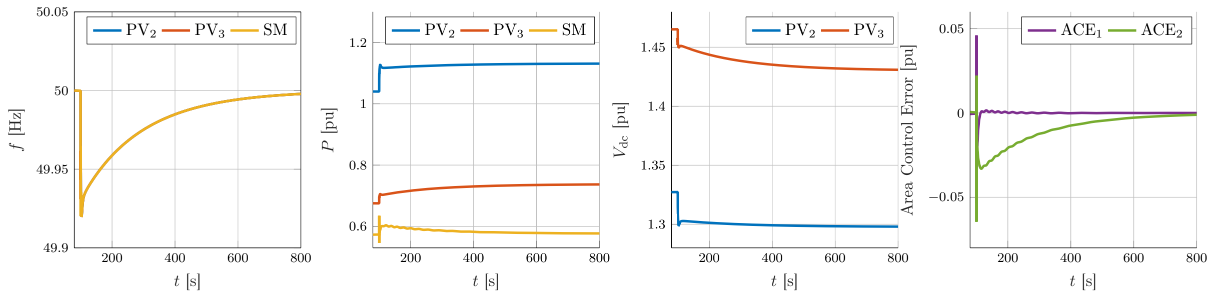

Figure 20: Simulation results for a $0.2\ \text{pu}$ load step at bus 7 of the power system ac 1 in Figure 16 with the HVDC link disconnected. The two voltage source converters participate in secondary control to return the system to nominal frequency.

The load step in Figure 21 exceeds the aggregate secondary control reserves $P_{\max,i}$ and the load returns to its nominal value at $t = 800\ \text{s}$. While the secondary controller does not return the system to its nominal frequency, the anti-windup feedback ensures stable operation of the system without integrator windup.

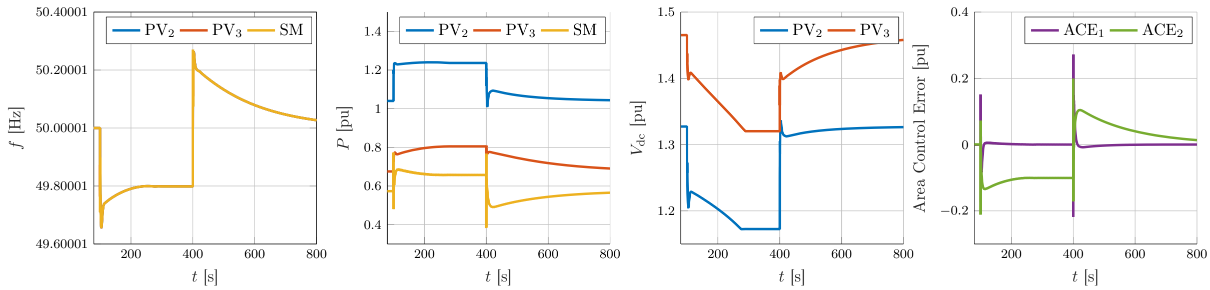

Figure 21: Simulation results for a $0.5\ \mathrm{pu}$ load step at bus 7 of the power system ac 1 in Figure 16 with the HVDC link disconnected. The system is divided into two areas (at bus 4). The two voltage source converters reach their power limit, control error in their area is not compensated, and a frequency offset and primary control response in the first area remain. The load returns to its nominal value at $t = 800\ \mathrm{s}$.

3.4 Flexibility and short-term energy storage of converter-interfaced renewable generation

In principle, the control algorithms presented in the previous sections enable a wide range of power electronic converters and renewable generation technologies to contribute to stabilizing large-scale power systems on time-scales from milliseconds to seconds. In this context, a key question is how much flexibility (i.e., curtailment of renewables) and short-term energy storage is required to satisfy standard performance specifications. Conceptually, a simple approach is to fully rely on energy storage to regulate the power output of renewable generation and provide frequency regulation services [48, 49, 50]. In the context of frequency stability and real-time control (i.e., up to the time-scales of secondary control), this requires establishing maximum credible contingencies (i.e., loss of generators, maximum fluctuations of renewable generation) and their duration, and sizing energy storage sytems to meet the resulting power and energy requirements. This problem is well understood for primary and secondary control in today's system. However, a less well understood problem is how the kinetic energy storage in today's system will be replaced. Moreover, the comparison presented in [51], suggests that energy storage is more expensive and less effective than deliberately operating PV generators below its Maximum Power Point (MPP). While a plethora of grid-following solutions exist [52, 53, 54], they only investigate individual grid-following power converters in isolation and do not clarify the system-level perspective.

Using standard grid-forming and grid-following control, the relationship between control gains, short-term energy storage, and the frequency response is difficult to quantify analytically and typically optimized using numerical tools (see, e.g., [12] for placement of virtual inertia). In contrast, the energy-balancing controller (36) makes the relationship between short-term energy storage of power converters (e.g., DC-link capacitor) and renewable generation (e.g., wind turbine rotor inertia), power generation time constants, and power generation sensitivities transparent.

To this end, we first note that the derivative term in (36) reduces the converter frequency and thereby its power injection if the DC voltage is dropping. This term realizes a function similar to that of damper windings in synchronous machines. For typical parameters values, m_p is an order of magnitude smaller than k_θ and the impact of this fast damping, analogously to the machine damper windings, is typically neglected on time-scales beyond a few cycles. Changing coordinates from DC voltage v to frequency ω and neglecting losses, the dynamics of a power converter with a DC power source (i.e., PV), can be expressed as

$$\frac{C}{k_\theta}\frac{\mathrm{d}}{\mathrm{d}t}\omega = -P_{\mathsf{ac}} + P, \tag{50a}$$

$$T_{\mathsf{g}}\frac{\mathrm{d}}{\mathrm{d}t}P = -P - \frac{k_{\mathsf{g}}}{k_\theta}\omega, \tag{50b}$$

i.e., the reduced-order model of a synchronous machine with turbine/governor system, equivalent inertia constant $\frac{C}{k_\theta}$, equivalent turbine constant T_{g}, and governor gain $\frac{k_{\mathsf{g}}}{k_\theta}$. It can be seen that a smaller control gain k_θ allows to tapping further into the DC storage, i.e., with smaller k_θ a given drop in frequency results in an increased drop in DC voltage and therefore releases more energy into the system. Moreover, the steady-state map from converter frequency deviations ω to DC voltage deviations is given by $\omega = k_\theta v$. In steady-state the converter frequency is synchronous with the system frequency and, letting $\Delta\omega_{\max}$ denote the largest frequency deviation for which primary control needs to be provided, the following constraints and specifications are obtained

$$k_\theta \leq \frac{\Delta\omega_{\max}}{v_{\mathsf{dc}}^\star - v_{\mathsf{dc}}^{\min}}, \tag{51a}$$

$$k_\theta \leq \frac{\Delta\omega_{\max}}{v_{\mathsf{dc}}^{\max}}, \tag{51b}$$

$$f_{\mathsf{dr}} = \frac{k_\theta}{k_{\mathsf{g}}(v_{\mathsf{dc}}^\star)}. \tag{51c}$$

The first constraint ensures that the DC voltage does not drop below its minimum (e.g., the MPP voltage $v_{\mathsf{dc}}^{\mathsf{MPP}}$ of PV), the second constraint ensures that the DC voltage does not exceed its maximum (e.g., the open circuit voltage of a PV panel), and the third equation specifies the droop percentage. We note that these three specifications are sometimes conflicting, i.e., depending on the power source sensitivity k_{g} the upper bound on k_θ may preclude achieving the desired droop percentage. In this case, one either needs to pick an operating point (i.e., curtailment) with increased sensitivity k_{g} and/or headroom or design the power converter to allow for larger DC voltage deviations.

Similar arguments can directly be applied to wind turbines with back-to-back power converter by considering the mapping of the system frequency through the back-to-back power converters to the wind turbine. In other words if $k_{\theta,g}$ denotes the gain of the grid side converter and $k_{\theta,r}$ denotes the gain of the rotor side converter, then, in steady-state the rotor speed deviation of the wind turbine would be given by $\omega_r = \frac{k_{\theta,g}}{k_{\theta,r}}\omega$ and the gains need to be selected such that, for the expected system frequency deviations, the rotor speed does not exceed its maximum speed, the rotor speed drops below the speed corresponding maximum power point, and the DC voltage stays within its limits. Moreover, the droop gain in this case is given by $\frac{k_{\mathsf{g}} k_{\theta,g}}{k_{\theta,r}}$. We note that, for typical wind turbine parameters and only using curtailment through the rotor speed, standard droop gains can often only be obtained in high wind speed scenarios. Finally, the equivalent inertia constant of a wind turbine as seen from the grid is also approximately scaled by $\frac{k_{\theta,g}}{k_{\theta,r}}$, typically resulting an increased inertia response (i.e., small system frequency deviations result in larger rotor speed deviations that in turn release / absorb more kinetic energy). This results in a significant inertia response by wind turbines when relying on the rotor speed for curtailment (see Figure 19).

Through this mechansim the requirements and curtailment for providing primary frequency control can directly be established and verified for each device. Another significant concern and focus of recent research, is the loss of synchronous machine inertia. Using the proposed control, the equivalent inertia constant of a voltage source converter is given by $\frac{C}{k_\theta}$ and the equivalent inertia of a machine with inertia m connected through back-to-back converters (e.g., wind turbine, flywheel) as seen from the system is given by $\frac{k_{\theta,g}}{k_{\theta,r}}m$. While the resulting equivalent inertia constant for power converters is still relatively small (e.g., on the order of $20\ \mathrm{ms}$ to $200\ \mathrm{ms}$), the equivalent inertia constant of wind turbines is significant (i.e., on the order of $10\ \mathrm{s}$ to $40\ \mathrm{s}$ depending on the wind turbine and curtailment strategy). Notably, this inertia is not virtual, but corresponds to actual energy storage in the grid that can therefore be sized accordingly (e.g., to size an ultracapacitor or flywheel energy storage system).

While these results show much of an inertia response can be provided by different devices, a more important question is how much inertia, if any, is needed in systems dominated by power electronics. Considering the equivalence between converters and machines established above, we will use the frequency dynamics of a machine with first order turbine governor model:

$$\tfrac{\mathrm{d}}{\mathrm{d}t}\theta = \omega, \tag{52a}$$

$$M\tfrac{\mathrm{d}}{\mathrm{d}t}\omega = -D\omega + P_s - P_e, \tag{52b}$$

$$T_s\tfrac{\mathrm{d}}{\mathrm{d}t}P_s = -P_s + K_D\omega, \tag{52c}$$

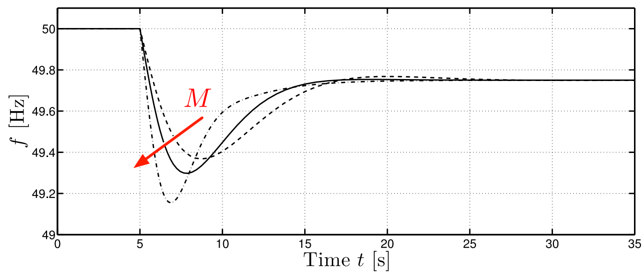

Figure 22: Typical response of a the system frequency of a multi-machine power system to a load step at $t = 5$s for different inertia constants M. The maximum RoCoF occurs at $t = 5$s and the frequency nadir is the minimum of the frequency after the load step. A decrease of the inertia constant M (for constant power source time constant T_s) results in an increased frequency deviation and RoCoF.

and standard power engineering metrics for frequency stability (i.e., the rate of change of frequency (RoCoF) and the frequency nadir). The rate of change of frequency is the derivative of the frequency with respect to time and the frequency nadir denotes the minimum of the frequency for a loss of generation or load step. In conventional systems these metrics are often evaluated using the so called center of inertia model in which a multi-machine system is replaced by a single equivalent machine model that models the collective frequency dynamics of the system [55].

For typical conventional power systems the response to a load step (i.e., a step increase in P_{ac}) is under-damped and shown in Figure 22 for different inertia constants M. As the inertia constant is decreased the frequency drops more rapidly and to lower values. This in line with the interpretation of the rotating mass as an energy buffer that supplies the load power until the turbine can increase its production and is the basis for the claim that a loss of rotational inertia will have significant negative impact frequency stability [2] and needs to be counteracted by inertia emulation. However, replacing synchronous machines with power converters not only removes the machines rotational inertia, but also replace the slow turbine (e.g., hydro and steam turbines) with power sources whose equivalent time constants T_s are orders of magnitude smaller. To clarify the role of the inertia constant, we note that the frequency nadir does not change if the time axis in Figure 22 is rescaled and propose to normalize time for the power source time constant, i.e., using the time $t' = t/T_s$. This results in

$$M/T_s \tfrac{\mathrm{d}}{\mathrm{d}t'}\omega = -D\omega + P_s - P_e, \tag{53a}$$
$$\tfrac{\mathrm{d}}{\mathrm{d}t'}P_s = -P_s + K_D\omega, \tag{53b}$$

In other words the normalized inertia constant is the ratio of the original inertia constant and the power source time constant. Applying the results from [55] to the the normalized system (53) it can be shown that the frequency nadir scales with ratio M/T_s, i.e., decreasing M/T_s increases the frequency nadir, while increasing M/T_s decreases the frequency nadir. In contrast, the maximum RoCoF directly scales with M. Figure 23 shows the impact of T_s and M_s in the original time coordinates. Loosely speaking, a smaller power source time constant results in frequency dynamics that evolve faster, while the inertia-to-power source time constant ratio determines the frequency nadir. Therefore, the approximate model suggests that decreasing both the inertia constant and the power source time constant does not affect the frequency nadir as long as M/T_s is constant. However, a lower power source time constant results in a system that evolves on a faster time scale and hence exhibits an increased maximum RoCoF. Figure 24 illustrates the frequency nadir and maximum averaged RoCoF for different inertia and power source time constants ranging from $10\mathrm{ms}$ (e.g., a PV system using energy-balancing control), $0.3\ \mathrm{s}$ (e.g., a wind turbine pitch actuator), to $\approx 7\mathrm{s}$ for steam turbines [56]. For reference, the grey area indicates typical values for today's large-scale multi-machine systems for a similar load step. It can be seen that today's values for the frequency nadir can be achieved at much lower inertia levels when using a control that fully leverages fast response capabilities of renewable power source and energy storage technologies. This result is in line with the EMT simulations shown in the previous section.

Overall, we draw several conclusions. For each power converter the equivalent inertia constant $\frac{C}{k_\theta}$

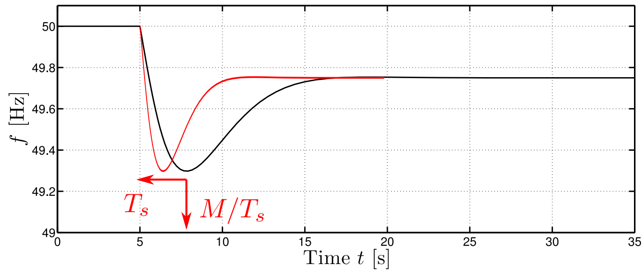

Figure 23: Typical response of a the system frequency of a multi-machine power system to a load step at $t = 5$s for different inertia constants M. The maximum RoCoF occurs at $t = 5$s and the frequency nadir is the minimum of the frequency after the load step. The system evolves on faster time scales if the power source time constant T_s is decreased and the frequency nadir scales mostly with the ratio M/T_s.

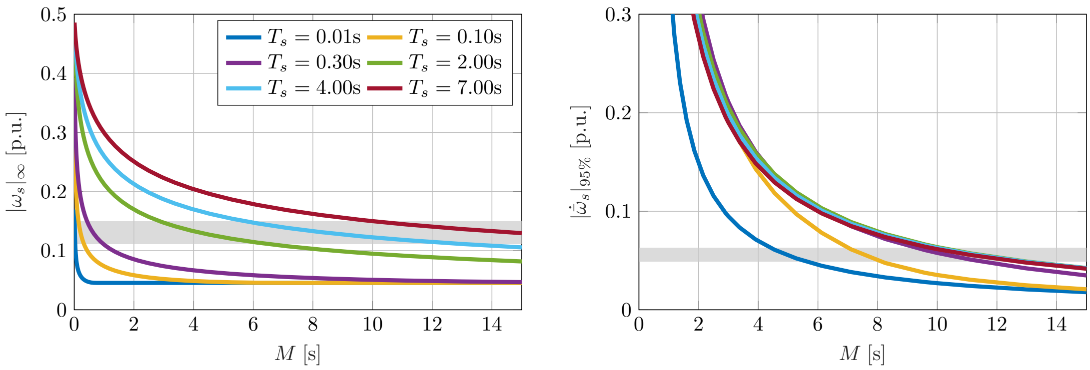

Figure 24: Frequency nadir $|\omega_s|_\infty$ and maximum of the averaged RoCoF $|\dot{\omega}_s|_{95\%}$ (averaged over $3T_s$) for a load step and different combinations of inertia and power source time constant. The shaded grey area denotes typical values for today's large-scale multi-machine systems for a comparable load increase. It can be seen that the frequency nadir is highly sensitive to the equivalent power source time constant T_s and the ratio M/T_s. In contrast, the averaged RoCoF mostly depends on the inertia constant M.

should be at least on the order of one to cycles to ensure a sufficient time-scale separation to the circuit dynamics. The ratios $\frac{C}{k_\theta T_{\mathrm{g}}}$ (for power converters) and $\frac{M}{T_{\mathrm{g}}}$ (for synchronous machines) needs to be large enough (e.g., larger than two to achieve the nadir specifications in Figure 24). Moreover, using the center of inertia frequency model is justified by the fact that energy-balancing control synchronizes all frequencies and DC voltages (see Figure 19) and the total inertia constant (i.e., sum of the device inertia constants) should be sufficiently large relative to the aggregate power source time constant. If the device power source time constants are approximately identical the aggregate power source time constant is identical to the device aggregate power source time constant. When the device power source time constants are heterogeneous scalable numerical model reduction methods can be used to identify the equivalent inertia time constant [57].

4 Conclusions

This project developed a unified grid-forming control and small-signal stability analysis framework that is applicable to a wide range of renewable generation technologies (e.g., wind turbines and photovoltaics), conventional technologies (e.g., synchronous generators and condensers) and other common actuators (e.g, HVDC). The control fully leverages the capabilities of each device and transparently incorporates device-level flexibility and short-term energy-storage. Moreover, converter-interfaced renewable generation using the proposed control can directly be integrated into prevailing secondary control mechanisms. The proposed approach reduces the complexity of system-level stability analysis by unifying standard control functions across different technologies and enabling a wide range of technologies to autonomous contribute to ensuring dynamic stability of future power systems. Moreover, it directly clarifies the trade offs between power generation flexibility, response time, and short-term energy storage of various devices from the perspective of frequency stability both at the device-level and system-level.

5 Outlook and next steps

While the control and small-signal stability analysis framework developed in this project can, conceptually, be applied to a wide range of technologies its performance and implications require further study in different application domains. For example, the control parameters for photovoltaics and wind turbines need to be adapted with changing solar irradiation or wind speeds. Moreover, further constraints need to be considered, for example wind turbines require auxiliary controls to maintain a safe rotor speed, and current limits of voltage source converters need to be accounted for to enable real-world applications of the results. Similarly, interactions with the protection system and a wider range of standard machine controls (e.g., power system stabilizers, AVRs) need to be investigated.

6 Publications and Dissemination

Journal publications and preprints

- I. Subotić, D. Groß: Power-balancing dual-port grid-forming power converter control for renewable integration and hybrid AC/DC power systems. Under review. Preprint: arXiv:2106.10396, 2021.
- D. Groß, E. Sánchez-Sánchez, E. Prieto-Araujo, O. Gomis-Bellmunt: Dual-port grid-forming control of MMCs and its applications to grids of grids. Under review. Preprint: arXiv:2106.11378, 2021.
- I. Subotić, D. Groß, M. Colombino, F. Dörfler: A Lyapunov framework for nested dynamical systems on multiple time scales with application to converter-based power systems. *IEEE Transactions on Automatic Control*, 2021.

Conferences and Workshops

- International Conference on Future Electric Power Systems and the Energy Transition, Champery, Switzerland, 2019.
- INFORMS annual meeting, 2019
- IEEE Power & Energy Society General Meeting, virtual, 2020.
- Computing in Engineering Forum, virtual, 2020.
- Conference on Information Sciences and Systems, virtual, 2021.
- NREL Resilient Autonomous Energy Systems workshop, virtual, 2021.

Seminar presentations

- Power Systems Engineering Center Summer Workshop, virtual, 2020.

- Wisconsin Public Utility Institute, virtual, 2020.
- North American Electric Reliability Corporation Inverter-Based Resource Performance Task Force meeting, virtual, 2020.
- Power Systems Engineering Center Webinar, 2021.
- Universal Interoperability for grid-Forming Inverters (UNIFI) Consortium, virtual, 2021.

References

[1] P. Tielens and D. V. Hertem, "The relevance of inertia in power systems," *Renewable and Sustainable Energy Reviews*, vol. 55, pp. 999–1009, 2016.

[2] W. Winter, K. Elkington, G. Bareux, and J. Kostevc, "Pushing the limits: Europe's new grid: Innovative tools to combat transmission bottlenecks and reduced inertia," *IEEE Power and Energy Magazine*, vol. 13, no. 1, pp. 60–74, 2015.

[3] A. Crivellaro, A. Tayyebi, C. Gavriluta, D. Groß, A. Anta, F. Kupzog, and F. Dörfler, "Beyond low-inertia systems: Massive integration of grid-forming power converters in transmission grids," in *IEEE PES General Meeting*, 2020.

[4] F. Milano, F. Dörfler, G. Hug, D. Hill, and G. Verbic, "Foundations and challenges of low-inertia systems," in *Power Systems Computation Conference*, 2018.

[5] U. Markovic, O. Stanojev, P. Aristidou, E. Vrettos, D. Callaway, and G. Hug, *IEEE Trans. Power Syst.*

[6] "Black system south australia 28 september 2016," Australian Energy Market Operator, Tech. Rep., 2017.

[7] "1,200 mw fault induced solar photovoltaic resource interruption disturbance report," North American Electric Reliability Corporation, Tech. Rep., 2017.

[8] A. Tayyebi, D. Groß, A. Anta, F. Kupzog, and F. Dörfler, "Frequency stability of synchronous machines and grid-forming power converters," *IEEE Trans. Emerg. Sel. Topics Power Electron.*, vol. 8, no. 2, pp. 1004–1018, 2020.

[9] O. Gomis-Bellmunt, E. Sánchez-Sánchez, J. Arévalo-Soler, and E. Prieto-Araujo, "Principles of operation of grids of DC and AC subgrids interconnected by power converters," *IEEE Trans. Power Del.*, vol. 36, no. 2, pp. 1107–1117, 2021.

[10] S.-K. Chung, "A phase tracking system for three phase utility interface inverters," *IEEE Transactions on Power Electronics*, vol. 15, no. 3, pp. 431–438, 2000.

[11] S. Golestan, M. Monfared, F. D. Freijedo, and J. M. Guerrero, "Performance improvement of a prefiltered synchronous-reference-frame PLL by using a PID-type loop filter," *IEEE Transactions on Industrial Electronics*, vol. 61, no. 7, pp. 3469–3479, 2014.

[12] B. K. Poolla, D. Groß, and F. Dörfler, "Placement and implementation of grid-forming and grid-following virtual inertia and fast frequency response," *IEEE Trans. Power Syst.*, vol. 34, no. 4, pp. 3035–3046, 2019.

[13] M. C. Chandorkar, D. M. Divan, and R. Adapa, "Control of parallel connected inverters in standalone AC supply systems," *IEEE Trans. Ind. Appl.*, vol. 29, no. 1, pp. 136–143, 1993.

[14] V. Mariani, F. Vasca, J. C. Vásquez, and J. M. Guerrero, "Model order reductions for stability analysis of islanded microgrids with droop control," *IEEE Trans. Ind. Electron.*, vol. 62, no. 7, pp. 4344–4354, 2015.

[15] J. W. Simpson-Porco, F. Dörfler, and F. Bullo, “Voltage stabilization in microgrids via quadratic droop control,” *IEEE Trans. Autom. Control*, vol. 62, no. 3, pp. 1239–1253, 2017.

[16] Q.-C. Zhong and G. Weiss, “Synchronverters: Inverters that mimic synchronous generators,” *IEEE Trans. Ind. Electron.*, vol. 58, no. 4, pp. 1259–1267, 2011.

[17] S. D’Arco, J. A. Suul, and O. B. Fosso, “A virtual synchronous machine implementation for distributed control of power converters in smartgrids,” *Electric Power Systems Research*, vol. 122, pp. 180–197, 2015.

[18] B. B. Johnson, S. V. Dhople, A. O. Hamadeh, and P. T. Krein, “Synchronization of parallel single-phase inverters with virtual oscillator control,” *IEEE Trans. Power Electron.*, vol. 29, no. 11, pp. 6124–6138, 2014.

[19] L. Tôrres, J. Hespanha, and J. Moehlis, “Synchronization of identical oscillators coupled through a symmetric network with dynamics: A constructive approach with applications to parallel operation of inverters,” *IEEE Trans. Autom. Control*, vol. 60, no. 12, pp. 3226–3241, 2015.

[20] D. Groß, M. Colombino, J.-S. Brouillon, and F. Dörfler, “The effect of transmission-line dynamics on grid-forming dispatchable virtual oscillator control,” *IEEE Trans. Control Netw. Syst.*, vol. 6, no. 3, pp. 1148–1160, 2019.

[21] I. Subotić, D. Groß, M. Colombino, and F. Dörfler, “A Lyapunov framework for nested dynamical systems on multiple time scales with application to converter-based power systems,” *IEEE Trans. Autom. Control*, vol. 66, no. 12, pp. 5909–5924, 2021.

[22] A. Ulbig, T. S. Borsche, and G. Andersson, “Impact of low rotational inertia on power system stability and operation,” in *IFAC World Congress*, vol. 47, no. 3, 2014, pp. 7290 – 7297.

[23] D. Groß, S. Bolognani, B. K. Poolla, and F. Dörfler, “Increasing the resilience of low-inertia power systems by virtual inertia and damping,” in *Bulk Power Systems Dynamics and Control Symposium (IREP)*, 2017.

[24] D. Groß, C. Arghir, and F. Dörfler, “On the steady-state behavior of a nonlinear power system model,” *Automatica*, vol. 90, p. 248–254, 2018.

[25] D. Groß and F. Dörfler, “On the steady-state behavior of low-inertia power systems.” *IFAC-PapersOnLine*, vol. 50, no. 1, pp. 10 735–10 741, 2017, 20th IFAC World Congress.

[26] S. Curi, D. Groß, and F. Dörfler, “Control of low-inertia power grids: A model reduction approach,” in *IEEE Conf. Decision and Control*, 2017, pp. 5708–5713.

[27] P. W. Sauer and M. A. Pai, *Power System Dynamics and Stability*. Prentice Hall, 1998.

[28] N. Pogaku, M. Prodanovic, and T. C. Green, “Modeling, analysis and testing of autonomous operation of an inverter-based microgrid,” *IEEE Trans. Power Electron.*, vol. 22, no. 2, pp. 613–625, 2007.

[29] D. Groß, E. Sánchez-Sánchez, E. Prieto-Araujo, and O. Gomis-Bellmunt, “Dual-port grid-forming control of MMCs and its applications to grids of grids,” 2021.

[30] G. Bergna-Diaz, J. A. Suul, and S. D’Arco, “Energy-based state-space representation of modular multilevel converters with a constant equilibrium point in steady-state operation,” *IEEE Trans. Power Electron.*, vol. 33, no. 6, pp. 4832–4851, 2018.

[31] E. Sánchez-Sánchez, D. Groß, E. Prieto-Araujo, F. Dörfler, and O. Gomis-Bellmunt, “Optimal multivariable mmc energy-based control for dc voltage regulation in hvdc applications,” *IEEE Trans. Power Del.*, 2019.

[32] IEEE Comittee Report, “Dynamic models for steam and hydro turbines in power system studies,” *IEEE Trans. Power App. Syst.*, vol. PAS-92, no. 6, pp. 1904–1915, 1973.

[33] J. Aho, A. Buckspan, J. Laks, P. Fleming, Y. Jeong, F. Dunne, M. Churchfield, L. Pao, and K. Johnson, “A tutorial of wind turbine control for supporting grid frequency through active power control,” in *American Control Conference*, 2012, pp. 3120–3131.

[34] Y. Jeong, K. Johnson, and P. Fleming, “Comparison and testing of power reserve control strategies for grid-connected wind turbines,” *Wind Energy*, vol. 17, no. 3, pp. 343–358, 2014.

[35] F. Pöschke, J. Fortmann, and H. Schulte, “Nonlinear wind turbine controller for variable power generation in full load region,” in *American Control Conference*, 2017, pp. 1395–1400.

[36] L. Holdsworth, J. B. Ekanayake, and N. Jenkins, “Power system frequency response from fixed speed and doubly fed induction generator-based wind turbines,” *Wind Energy*, vol. 7, no. 1, pp. 21–35, 2004.

[37] K. V. Vidyanandan and N. Senroy, “Primary frequency regulation by deloaded wind turbines using variable droop,” *IEEE Trans. Power Syst.*, vol. 28, no. 2, pp. 837–846, 2013.

[38] S. Georg, H. Schulte, and H. Aschemann, “Control-oriented modelling of wind turbines using a takagi-sugeno model structure,” in *IEEE International Conference on Fuzzy Systems*, 2012.

[39] Y. Ma, A. Huang, and X. Zhou, “A review of STATCOM on the electric power system,” in *IEEE International Conference on Mechatronics and Automation (ICMA)*, 2015, pp. 162–167.

[40] I. Cvetkovic, D. Boroyevich, R. Burgos, C. Li, and P. Mattavelli, “Modeling and control of grid-connected voltage-source converters emulating isotropic and anisotropic synchronous machines,” in *IEEE Workshop on Control and Modeling for Power Electronics (COMPEL)*, 2015.

[41] T. Knudsen and T. Bak, “Simple model for describing and estimating wind turbine dynamic inflow,” in *American Control Conference*, 2013, pp. 640–646.

[42] P. Monshizadeh, C. De Persis, T. Stegink, N. Monshizadeh, and A. van der Schaft, “Stability and frequency regulation of inverters with capacitive inertia,” in *IEEE Conf. on Dec. and Contr.*, 2017, pp. 5696–5701.

[43] R. Pates and E. Mallada, “Robust scale-free synthesis for frequency control in power systems,” *IEEE Trans. Control Netw. Syst.*, vol. 6, no. 3, pp. 1174–1184, 2019.

[44] I. Subotić and D. Groß, “Power-balancing dual-port grid-forming power converter control for renewable integration and hybrid AC/DC power systems,” 2021.

[45] J. Sabatier, T. Youssef, and M. Pellet, “HVDC line parameters estimation based on line transfer functions frequency analysis,” in *Int. Conf. on Informatics in Control, Automation and Robotics*, 2015, pp. 497–502.

[46] E. Weitenberg, Y. Jiang, C. Zhao, E. Mallada, C. De Persis, and F. Dörfler, “Robust decentralized secondary frequency control in power systems: Merits and tradeoffs,” *IEEE Trans. Autom. Control*, vol. 64, no. 10, pp. 3967–3982, 2019.

[47] C. Konstantinopoulos, I. Avramiotis-Falireas, S. Bolognani, D. Groß, A. Chacko, and G. Hug, “Reliability assessment of pv units in primary and secondary frequency control ancillary services,” in *European Energy Market Conference*, 2019.

[48] N. Kakimoto, S. Takayama, H. Satoh, and K. Nakamura, “Power modulation of photovoltaic generator for frequency control of power system,” *IEEE Trans. Energy Convers.*, vol. 24, no. 4, pp. 943–949, 2009.

[49] R. Bhatt and B. Chowdhury, “Grid frequency and voltage support using PV systems with energy storage,” in *North American Power Symp.*, 2011.

[50] C. A. Hill, M. C. Such, D. Chen, J. Gonzalez, and W. M. Grady, “Battery energy storage for enabling integration of distributed solar power generation,” *IEEE Trans. Smart Grid*, vol. 3, no. 2, pp. 850–857, 2012.

[51] W. A. Omran, M. Kazerani, and M. M. A. Salama, “Investigation of methods for reduction of power fluctuations generated from large grid-connected photovoltaic systems,” *IEEE Trans. Energy Convers.*, vol. 26, no. 1, pp. 318–327, 2011.

[52] V. A. K. Pappu, B. Chowdhury, and R. Bhatt, “Implementing frequency regulation capability in a solar photovoltaic power plant,” in *North American Power Symposium*, 2010.

[53] H. Xin, Y. Liu, Z. Wang, D. Gan, and T. Yang, “A new frequency regulation strategy for photovoltaic systems without energy storage,” *IEEE Trans. Sustain. Energy*, vol. 4, no. 4, pp. 985–993, 2013.

[54] H. D. Tafti, A. I. Maswood, G. Konstantinou, J. Pou, and F. Blaabjerg, “A general constant power generation algorithm for photovoltaic systems,” *IEEE Trans. Power Electron.*, vol. 33, no. 5, pp. 4088–4101, 2018.

[55] F. Paganini and E. Mallada, “Global analysis of synchronization performance for power systems: Bridging the theory-practice gap,” *IEEE Transactions on Automatic Control*, vol. 65, no. 7, pp. 3007–3022, 2020.

[56] P. Kundur, *Power system stability and control*. McGraw-Hill, 1994.

[57] H. Min, F. Paganini, and E. Mallada, “Accurate reduced-order models for heterogeneous coherent generators,” *IEEE Control Syst. Lett.*, vol. 5, no. 5, pp. 1741–1746, 2021.